PCM1 orchestrates centrosomal and flagellar protein transport to promote sperm maturation

Check for updates

Zicong Huang[1,8], Runduan Yi [1,8], Xixian Cen [1,8], Hanbin Zhang[2], Minyu Xie[2], Ke Ma[1], Shipeng Ruan [1], Yuge Zhuang [1], Xiaoyuan Zhang [1], Wenyuan Liu [1], Hongrui Feng [1], Deyu Chen[3], Mohamed Morsi M. Ahmed[4], Hong Liu [5,9] ✉, Chuyu Huang [6,9] ✉, Xiangjin Kang [2,9] ✉ & Zhenguo Chen [1,7,9] ✉

Centriolar satellites facilitate the delivery of proteins required for centrosome assembly and function, and rely on the nucleation of the scaffold protein pericentriolar material 1 (PCM1). During sperm maturation, centrosomes undergo remodeling to facilitate neckpiece formation and flagellogenesis. However, the role and mechanism of PCM1 in centrosome remodeling and sperm maturation remain to be elucidated. Herein we show that PCM1 is downregulated in patients with non-obstructive azoospermia. *Pcm1* knockout mice exhibit disrupted spermiogenesis, characterized by a disorganized manchette and head-tail coupling apparatus, defective flagellogenesis, and male infertility. Mechanistically, PCM1 binds centrosomal proteins and governs their precise translocation via intra-manchette transport, ensuring proper centrosome remodeling and axoneme biogenesis. Inactivation of PCM1 in sperm leads to severe retardation of embryo development, which cannot be overcome by intra-cytoplasmic sperm injection. Collectively, these findings establish PCM1 as a key regulator of spermatogenesis and spermiogenesis, highlighting the contribution of sperm centrosome-related proteins to embryo development and fertility.

Infertility is a prevalent condition affecting an estimated 70 million people, with approximately 15% of couples struggling with fertility issues worldwide, and male factor infertility accounts for approximately 50% of affected couples[1,2]. Azoospermia and oligoasthenoteratozoospermia represent major causes of male infertility resulting from severe impairment of spermatogenesis. Although some genetic causes for azoospermia and oligoasthenoteratozoospermia have been established, there are still many idiopathic cases[3,4]. Spermatogenesis is a complicated process that can be divided into three phases (mitotic, meiotic, and haploid)[5–7]. Severe disruptions in the mitotic or meiotic phase tend to impair spermatogenesis and cause azoospermia, whereas disorders in the haploid phase (spermiogenesis) often lead to a reduced sperm count, malformed spermatozoa, and compromised sperm motility (oligoasthenoteratozoospermia)[1,5,7,8]. Throughout the process of human spermiogenesis, >4000 genes have been shown to anticipate the dynamic morphologic alterations of spermatids, which include nuclear condensation and head shaping, formation of the acrosome and flagella, and elimination of cytoplasm, eventually transforming into spermatozoa[9–11]. However, the molecular mechanisms underlying spermiogenesis have not been completely understood.

During spermiogenesis, centrioles and their surrounding pericentriolar material undergo a transformation process (centrosome remodeling), which involves translocation of the proximal centriole beneath the nucleus, conversion of pericentriolar materials into the capitulum and segmented column that are tightly attached to the basal plate, and the distal centriole that serves as the basal body for axoneme biogenesis. The well-organized structure (head-tail coupling apparatus [HTCA]) tightly connects the sperm head and flagellum and is crucial for sperm maturation and motility[12]. Emerging evidence has shown that dysfunction of the centrosomal proteins (POC1A or CETN1 [centrin1]) results in male factor infertility in mice[13,14]. Additionally, centrosomal proteins (CEPs), including CEP135, CEP70 and CEP78, and centriolar satellite protein CEP131, play critical roles in spermiogenesis[15–20]. Dysfunction of these proteins in humans or mice results in abnormal spermatid centriole formation, aberrant manchette organization, and flagellar structures. Consequently, sperm motility and male fertility are largely impaired. Of note, centrioles are profoundly degenerated during spermatid maturation in mice but largely retained in human[21]. To date, the molecular networks monitoring centrosome remodeling to ensure correct spermiogenesis have not been elucidated.

Centriolar satellites are small, dynamic granules, approximately 70–100 nm in diameter, that traffic along cytoplasmic microtubules to and from the centrosome and the ciliary base[22]. These satellites play a critical role in regulating centrosome composition and facilitating protein delivery required for centrosome and cilia function[23,24]. As the marker of centriolar satellites, pericentriolar material 1 (PCM1) is considered the principal scaffold protein for satellite assembly, which is involved in the microtubule- and dynactin-dependent recruitment of proteins and participates in centrosome integrity and microtubule dynamics[25,26]. PCM1 also plays a pivotal role in ciliogenesis by sequestering proteins in the centriolar satellite compartment[27]. Depletion of *Pcm1* in cells disassembles centriolar satellites, leading to the degradation of several satellite components, including key ciliary proteins, and prevents the formation of primary cilia by disrupting the microtubule network and protein trafficking[28]. Specifically, remodeling of the mother centriole due to defective removal of CP110 and CEP97 from the mother centriole[28], and defective IFT88 recruitment to basal body and cilia[29], partly explain the underlying mechanism. Interestingly, the *Pcm1* knockout mice exhibited reduced sperm count[28], indicating that PCM1 dysfunction affects not only ciliogenesis but also spermatogenesis. To date, no *PCM1* mutation has been identified linking to human diseases, including infertility, although some *PCM1* variants are suggested to contribute to a risk for schizophrenia[30]. The specific function and molecular mechanisms by which PCM1 regulates spermatogenesis and/or spermiogenesis remain poorly understood and warrant further investigation.

Herein, we showed that the PCM1 protein level was significantly decreased in patients with non-obstructive azoospermia (NOA [representing defective spermatogenesis]) compared to patients with obstructive azoospermia (OA [representing normal spermatogenesis]). *Pcm1* knockout (*Pcm1*−/−) mice exhibited severe oligoasthenoteratozoospermia and male factor infertility that represented the syndromes observed in clinical patients. PCM1 mediates the translocation of centrosomal and flagellar proteins primarily through intra-manchette transport to ensure correct centrosome remodeling and axoneme biogenesis. Notably, *Pcm1*−/− sperm cannot support embryo development when injected into wild-type eggs via intracytoplasmic sperm injection (ICSI). Together, our findings unravel the role and mechanism underlying PCM1 in spermatogenesis, spermiogenesis, and embryonic development.

Results

PCM1 is involved in spermatogenesis

To screen the genes for which the altered expression is involved in spermatogenic defects, testes biopsies were obtained from NOA (severe spermatogenic defects, no spermatids or sperm) and OA (normal spermatogenesis, tubular lumen obstruction) patients for proteomics analyses (Supplementary Fig. 1a), using isobaric tags for relative and absolute quantification (iTRAQ) analysis. Among the differentially expressed proteins (DEPs), PCM1 exhibited significantly lower protein levels in the NOA group compared to the OA group (Table 1 and Supplementary Table 1). To confirm this finding, we performed immunohistochemical (IHC) staining of PCM1 on a section of the testis biopsy tissue microarray containing 30 NOA and 25 OA samples (Supplementary Fig. 1b). Expression intensity ranking and analysis (described in Materials and methods) confirmed that the PCM1 protein levels were significantly decreased in the NOA testes (Table 2), suggesting a potential implication of PCM1 dysfunction in spermatogenic defects.

To define the role of PCM1 in spermatogenesis, IHC staining was performed to monitor the temporal and spatial expression profile of PCM1 in wild-type (WT) mouse testes. PCM1 expression was low in postnatal day 1 testis, then increased progressively, and reached a peak at adult (Fig. 1a, b and Supplementary Fig. 2a). Immunofluorescent staining demonstrated robust PCM1 expression in the cytoplasm of meiotic spermatocytes in adult testicular sections, while weaker but detectable signals were also present in both round and elongating/elongated spermatids (Fig. 1c), indicating that PCM1 is involved in spermatogenesis and spermiogenesis. Furthermore, round and elongating spermatids were isolated from WT mouse testes (steps 1–14) and co-stained PCM1 with α-tubulin or peanut agglutinin (PNA [a marker labeling the outer acrosomal membrane]; Fig. 1d, e). PCM1 displayed a cytoplasmic localization in round and elongating spermatids, mostly localizing at or near microtubules marked with α-tubulin, then relocalizing from uniform distribution to concentrate at the cauda part at advanced stage. While it showed a weak association with the acrosome (Fig. 1d, e). Besides, strong PCM1 signals were also detected in the head, neck, and midpiece parts of mature sperm in humans, mice, and rats (Fig. 1f and Supplementary Fig. 2b, c), indicating that PCM1 may also have a role in sperm function. Taken together, these data suggest that PCM1 has a role in spermatogenesis and sperm maturation, possibly involving an association with the microtubule system.

Knockout of *Pcm1* causes pubertal growth retardation and lethality

To confirm that PCM1 downregulation is the real cause for spermatogenic defects, and to characterize the physiologic functions of PCM1 in spermatogenesis and spermiogenesis, *Pcm1* knockout mice (*Pcm1*−/−) were generated using the CRISPR/Cas9 system to delete exons 3–6 of the *Pcm1* gene, which resulted in a frameshift mutation and disruption of protein expression (Supplementary Fig. 2d, e). Genotyping via PCR analyses confirmed Mendelian inheritance and *Pcm1*−/− mice with the correct genotype were obtained (Supplementary Fig. 2f). Immunofluorescence showed that PCM1 signals were completely cleared in the *Pcm1*−/− testes (Fig. 2a), confirming the successful elimination of PCM1 proteins.

Pcm1−/− males and females collectively showed abnormal early lethality at 2–8 weeks of age (Fig. 2b). Physical development was retarded in the survivors of both sexes for 3 weeks of age but was recovered after 6 weeks of age (Fig. 2c, d and Supplementary Fig. 2c, d). These observations were consistent with a recent study investigating the role of PCM1 in ciliogenesis[28]. Further studies are needed to elucidate the precise molecular mechanisms underlying this phenomenon.

Deletion of *Pcm1* causes severe oligoasthenoteratospermia and male infertility

It was previously shown that *Pcm1*−/− male mice exhibited reduced sperm number[28], while the exact function and mechanism underlying PCM1 in spermatogenesis and male fertility have not been characterized. Therefore, the effects of *Pcm1* deletion on testis development and spermatogenesis were thoroughly examined. Although the size and mass of the testes and epididymides were not altered (Fig. 2d–f), *Pcm1*−/− testes appeared to have thinner epithelia and larger lumen in tubules, indicative of germ cell loss (Fig. 2g). Indeed, mature sperm were rarely observed in *Pcm1*−/− cauda

Table 1 | iTRAQ analysis reveals the relative protein levels of PCM1 in three paired testis biopsies (NOA vs. OA)

Test-1	Test-2	Test-3	Average	Coefficient of variation	Fold_change
0.2051	0.3076	0.2466	0.2531	0.2037	−3.95

Test-1, -2, -3 indicate three tests with three randomly paired samples (NOA vs. OA). Fold_change ≤−1.5 is considered significantly downregulated.
AVG average, *CV* coefficient of variation.

Table 2 | PCM1 expression ranking in a tissue microarray containing 30 NOA and 25 OA testis biopsies

Expression intensity	NOA	OA	*p* value
Negative (−)	5/30	13/25	*p* = 0.003
Weakly positive (+)	9/30	7/25	
Moderately positive (++)	13/30	4/25	
Strongly positive (+++)	3/30	1/25	

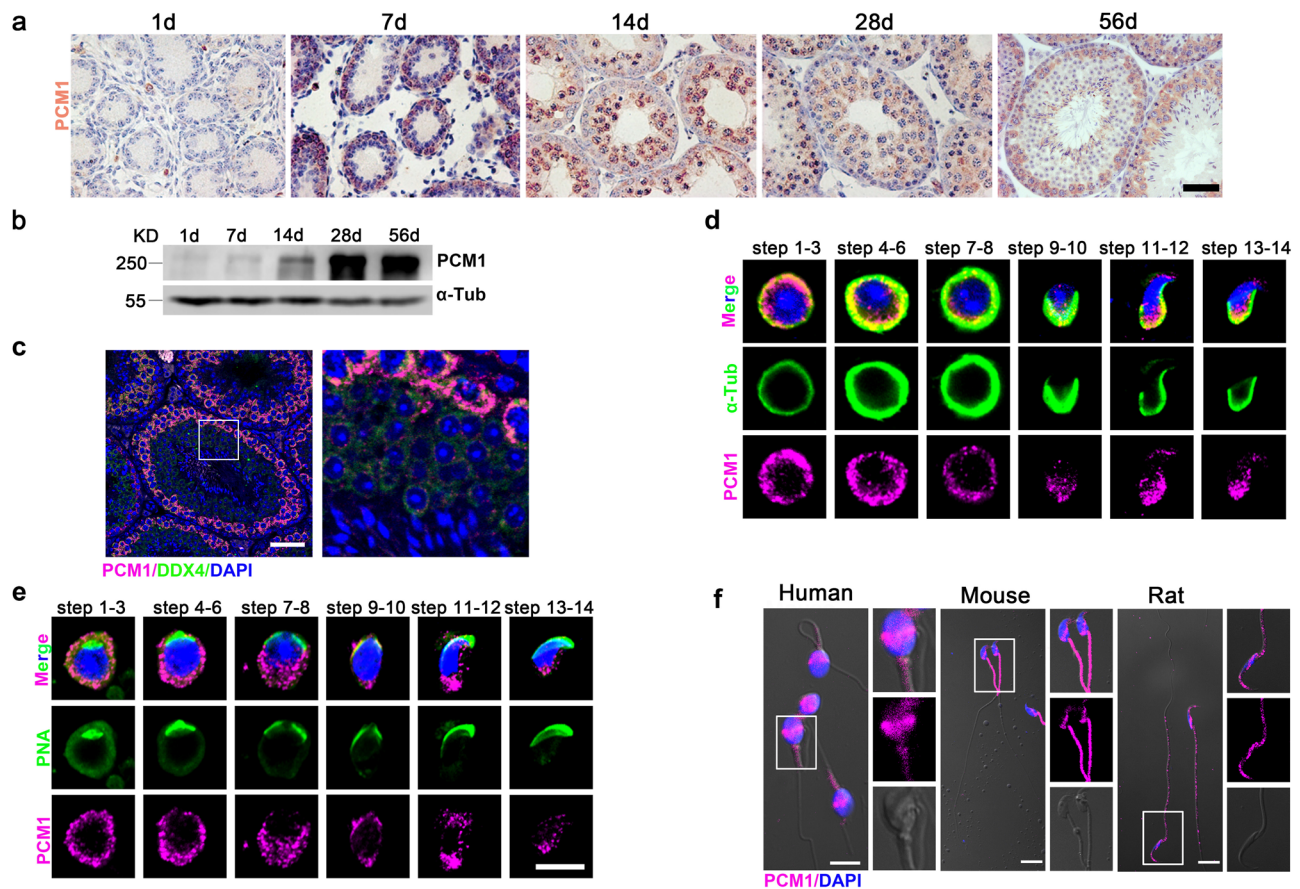The differences in the *PCM1* expression between groups were tested using the Wilcoxon signed-rank test.

Fig. 1 | PCM1 is involved in spermatogenesis. a IHC staining showing the temporal and spatial expression profile of PCM1 in the testes of mice at the key ages of 1, 7, 14, 28 and 56 days after birth. Scale bars: 20 μm. **b** Western blotting analyses of PCM1 expression in mouse testes. 1-, 7-, 14-, 28-and 56-d-old WT mice were analyzed. **c** Co-immunostaining of PCM1 (magenta) and DDX4 (green), a germ cell marker, in the testis of 10-week-old WT mice. Scale bars: 10 μm. Dynamic distributions of PCM1 (magenta) and α-tubulin (**d**, green), and PNA (**e**, green, labeling acrosome) at different steps during spermatid extension. Individual spermatids were dissected from 10-week-old WT mouse testes. Scale bars: 10 μm. **f** Immunostaining of PCM1 (magenta) in epididimal spermatozoa from human, mouse or rat. Scale bars: 5 μm, 10 μm, 10 μm.

epididymides (Fig. 2h). Notably, sperm concentration was decreased by approximately 99% (Fig. 2i) and sperm motility was decreased by approximately 75% in $Pcm1^{-/-}$ males (Fig. 2j, Table 2 and Supplementary Videos 1 and 2). Additionally, 88% of the remaining sperm exhibited a morphologic abnormality (Fig. 2k and Supplementary Table 2), which was mainly characterized by immature round spermatids, and deformed sperm heads or tails. Scanning electron microscopy identified severely distorted heads and/or enlarged cytoplasmic droplet-like structures in $Pcm1^{-/-}$ sperm (Fig. 2l and Supplementary Table 2). As a result, $Pcm1^{-/-}$ males did not impregnate any WT C57 females during a 6-month period of mating. These results demonstrated that loss of $Pcm1$ leads to severe oligoasthenoteratospermia and male factor infertility.

Ablation of *Pcm1* impairs spermatogenesis and spermiogenesis
Loss of $Pcm1$ was thought to perturb the development and differentiation of germ cells. Immunofluorescence of DDX4 revealed that germ cells were significantly decreased in $Pcm1^{-/-}$ testes (Fig. 3a, d). In addition, $Pcm1^{-/-}$ testes showed increased immunofluorescent signals of γH2AX, a marker for unrepaired DNA lesions, suggesting that $Pcm1$ deletion caused more damage to the germ cells (Fig. 3b, e). The TUNEL assay demonstrated a considerable increase in apoptotic cells in $Pcm1^{-/-}$ tubules (Fig. 3c, f). These results added credence to the notion that PCM1 is essential for spermatogenesis.

Next, spermiogenesis was analyzed in $Pcm1^{-/-}$ testes. Immunofluorescence of acetylated α-tubulin (Ac-tubulin), which marks flagellar axonemes, confirmed that while $Pcm1^{+/+}$ tubule lumens were filled with

sperm flagella, very few sperm flagella were present in $Pcm1^{-/-}$ tubules (Fig. 3g). Periodic acid-Schiff (PAS) staining further confirmed a thinner epithelium and a less flagella-filled lumen in $Pcm1^{-/-}$ tubules (Fig. 3h). Light microscopy revealed the pre-spermiogenic stages of spermatogenesis, up to step 7–8 spermatids, appeared to be normal, while the mutant elongating spermatids were frequently mis-localized or mis-orientated within the epithelia (Supplementary Fig. 3a). By dissecting individual spermatids, $Pcm1^{-/-}$ elongating spermatids were shown to have notable abnormal head and acrosome morphologies after spermatogenic step 9 (Fig. 3i and Supplementary Fig. 3a). Finally, $Pcm1^{-/-}$ elongated spermatids (steps 15–16) exhibited abnormal club-shaped nuclear morphology in sharp contrast to the normal hook-shaped nuclei in $Pcm1^{+/+}$ spermatids (Fig. 3i and Supplementary Fig. 3a). These observations suggested that PCM1 is necessary for spermiogenesis.

In addition, α-tubulin formed a regular cone-shaped structure surrounding the nucleus in $Pcm1^{+/+}$ elongating spermatids, which corresponded to the manchette organization in shaping the head, along with a normal cap-like acrosomal morphology. In contrast, all of these were notably deformed in the $Pcm1^{-/-}$ spermatids (Supplementary Fig. 3b). Very few spermatids reached maturity or successfully entered the epididymis, some of which even exhibited various types of malformations, which was consistent with our above observations (Fig. 2e–l, Supplementary Tables 2 and 3 and Supplementary Videos 1 and 2). Taken together, these results demonstrated that PCM1 is indispensable for spermatogenesis and spermiogenesis, and PCM1 dysfunction leads to severe oligoasthenoteratospermia and male factor infertility.
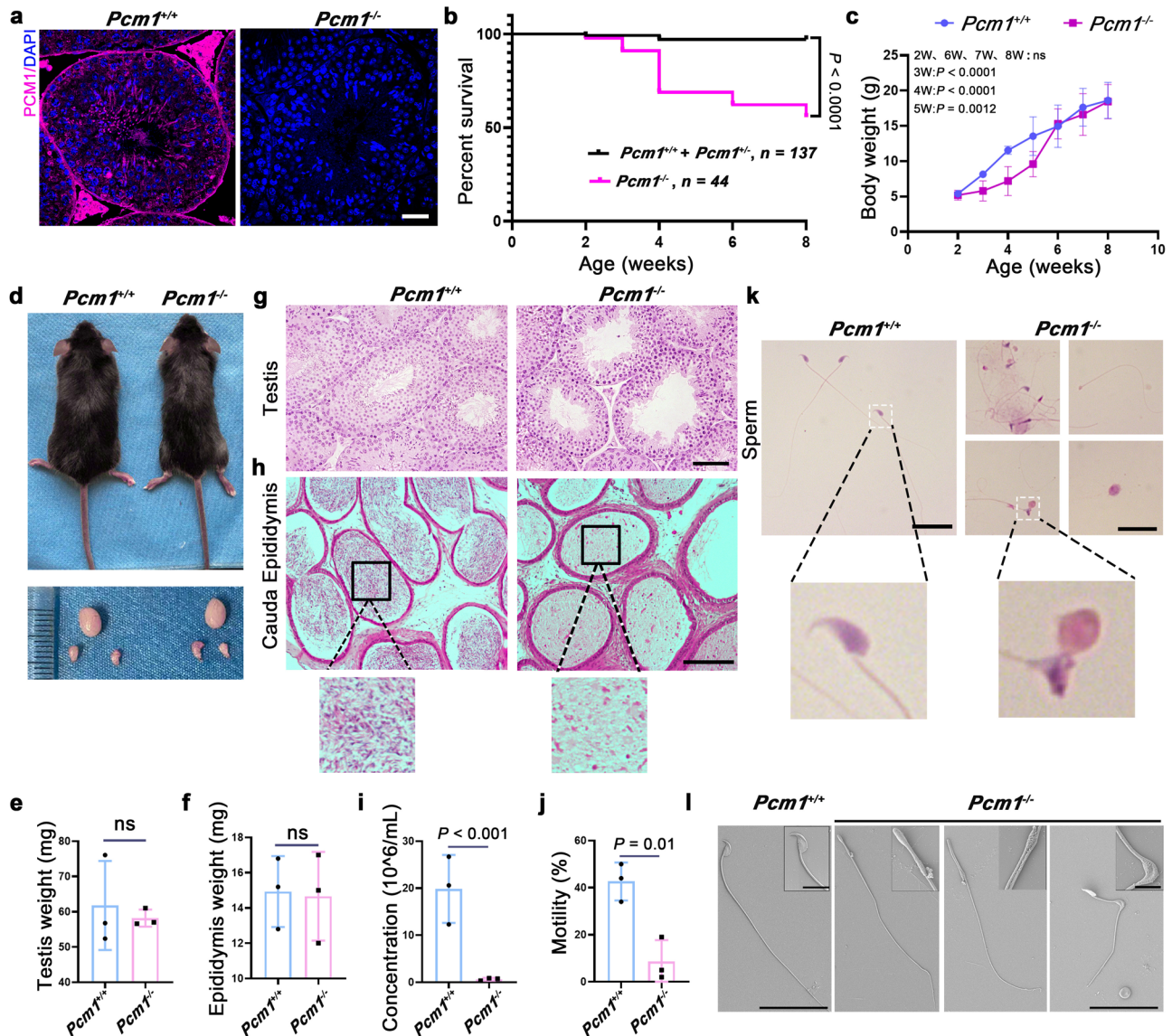
Fig. 2 | Knockout of *Pcm1* causes pubertal lethality and oligoasthenoteratospermia in mice. a Immunostaining of PCM1 in the seminiferous tubule of 10-week-old *Pcm1*⁺/⁺ and *Pcm1*⁻/⁻ mice. Scale bars: 20 μm. **b** Survival curve of the *Pcm1*⁺/⁺ and *Pcm1*⁻/⁻ mice. Both sexes were included. **c** Developmental curves shown as body weights of the *Pcm1*⁺/⁺ and *Pcm1*⁻/⁻ mice at indicated ages. *n* = 10 for each group. Both sexes were included. **d** Representative images showing overall views of body, testis and epididymitis. **e**, **f** Comparison of testis and epididymis weight. **g**, **h** H&E staining showed the histomorphology of testis and epididymis. Scale bars: 50 μm for testis, 100 μm for epididymis. **i**, **j** Sperm concentration and motility measured by CASA. **k** H&E staining showed various morphological abnormalities of the *Pcm1*⁻/⁻ spermatozoa. Scale bars: 50 μm. **l** Scanning electron microscopy confirmed malformation of the *Pcm1*⁻/⁻ spermatozoa. Distorted heads and/or enlarged cytoplasmic droplet-like structures in *Pcm1*⁻/⁻ sperm. Mice used were 10 weeks old. Data were presented as Mean ± SD. *n* = 3 except *n* = 10 in (**c**). *t*-test was used for comparing two groups except that the data presented as percentage or ratio were analyzed by the Chi square test.

Loss of *Pcm1* disrupts spermatid head shaping, neckpiece development, and flagellar formation

During spermatid elongation, the nucleus undergoes chromatin condensation, excess cytoplasm is removed, and a functional acrosome and sperm tail are formed[31]. The manchette has a critical role in these processes. To gain an overall perception on spermatid differentiation defects induced by PCM1 deficiency, the acrosome biogenesis process, which is divided into Golgi, cap, acrosome, and maturation phases, was analyzed by performing co-immunofluorescence of PNA and Ac-Tubulin to label the stabilized tubulins in the manchette. Dynamic manchette organization and acrosomal biogenesis with *Pcm1*⁺/⁺ spermatids maturation were observed and significantly disrupted in *Pcm1*⁻/⁻ spermatids, characterized by shrunken acrosomal vesicles at the cap phase, malformed acrosome and disorganization of the manchette at the acrosome phase, and a misshapen

nucleus and acrosome absence (Supplementary Fig. 3c). To further elucidate the detailed structural defects underlying these disorders, transmission electron microscopy (TEM) was used to decipher the spermatid elongation step-by-step. Each acrosome phase was clearly observed in *Pcm1*⁺/⁺ spermatids (Fig. 4a, c, e, g). *Pcm1*⁺/⁺ spermatids underwent dramatic but regular changes by the acrosomal phase, including progressive head shaping and nuclear condensation, an evenly-distributed perinuclear ring, a well-organized manchette tightly aligned along the nucleus, and a clear implantation fossa (Fig. 4e). In contrast, *Pcm1*⁻/⁻ spermatids showed an aberrantly extended and elongated manchette, an asymmetric perinuclear ring, a misshapen nucleus, and a deformed acrosome along with a thickened acroplaxome (Fig. 4f). Consequently, the nucleus of *Pcm1*⁻/⁻ elongated spermatids cannot regularly compact and the head and acrosome were quite malformed (Fig. 4h). Even though nuclear condensation appeared ongoing,
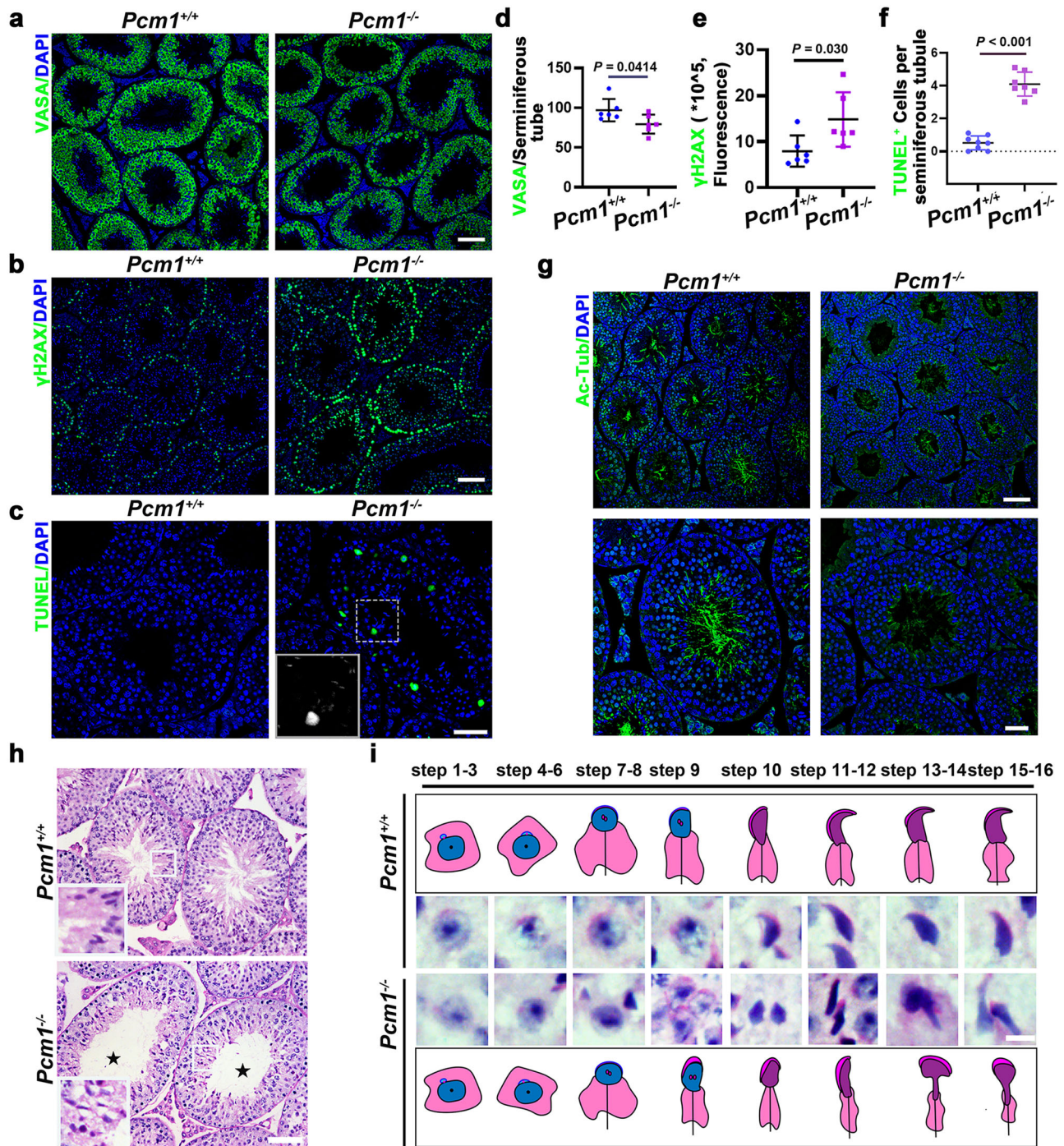
Fig. 3 | Deletion of *Pcm1* impairs spermatogenesis and spermiogenesis.
a Immunostaining of DDX4 (green) to label germ cells in *Pcm1*⁺/⁺ and *Pcm1*⁻/⁻ testes. Scale bars: 50 μm. **b** Immunostaining of γH2AX (green) showed germ cell injuries in *Pcm1*⁺/⁺ and *Pcm1*⁻/⁻ testes. Scale bars: 50 μm. **c** TUNEL (green) assay showed germ cell apoptosis in *Pcm1*⁺/⁺ and *Pcm1*⁻/⁻ testes. Scale bars: 10 μm. **d** Quantification of DDX4 fluorescence in (**a**), n = 6 for each group. **e** Quantification of γH2AX fluorescence in (**b**), n = 6 for each group. **f** Quantification of TUNEL-positive cells in seminiferous tubules. n = 8. **g** Immunofluorescence of acetylated tubulin (Ac-Tub, green) to label spermatid flagella in the seminiferous tubules of *Pcm1*⁺/⁺ and *Pcm1*⁻/⁻ mice. Scale bars: 50 μm (up), 20 μm (down). **h** PAS staining of testes sections showed enlarged lumen and absence of flagella in the *Pcm1*⁻/⁻ tubules. Scale bars: 20 μm. **i** PAS staining of spermatids at different steps from the *Pcm1*⁺/⁺ and *Pcm1*⁻/⁻ mice. Notable morphological abnormalities in the *Pcm1*⁻/⁻ spermatids were first seen at step 9. Scale bars: 5 μm. Blue indicate nuclei stained with DAPI. Mice used were 10 weeks old. Data were presented as Mean ± SD. *t*-test was used for comparing two groups.

the head shaping, acrosome extension, and cytoplasmic removal were still blocked (Fig. 4). TEM analyses detected a well-structured mitochondrial sheath in epididymal spermatozoa encircling nine out dense fibers (ODF) and the axoneme, comprising the typical "9 + 2" microtubules in the *Pcm1*⁺/⁺ sperm flagella (Fig. 4j, m). A considerable proportion of *Pcm1*⁻/⁻ flagella exhibited incomplete mitochondrial sheaths (20.18%) and ODF

(12.84%, Fig. 4k, l). Notably, the typical "9 + 2" microtubules were absent in 23.85% *Pcm1*⁻/⁻ sperm, and an aberrant "6 + 2" or "8 + 2" microtubular composition was frequently observed (Fig. 4n, o).

During mammalian spermiogenesis, the centrosome is remodeled where centrosomal proteins are removed, decreased, enriched, or redistributed to facilitate assembly of the HTCA and initiation of
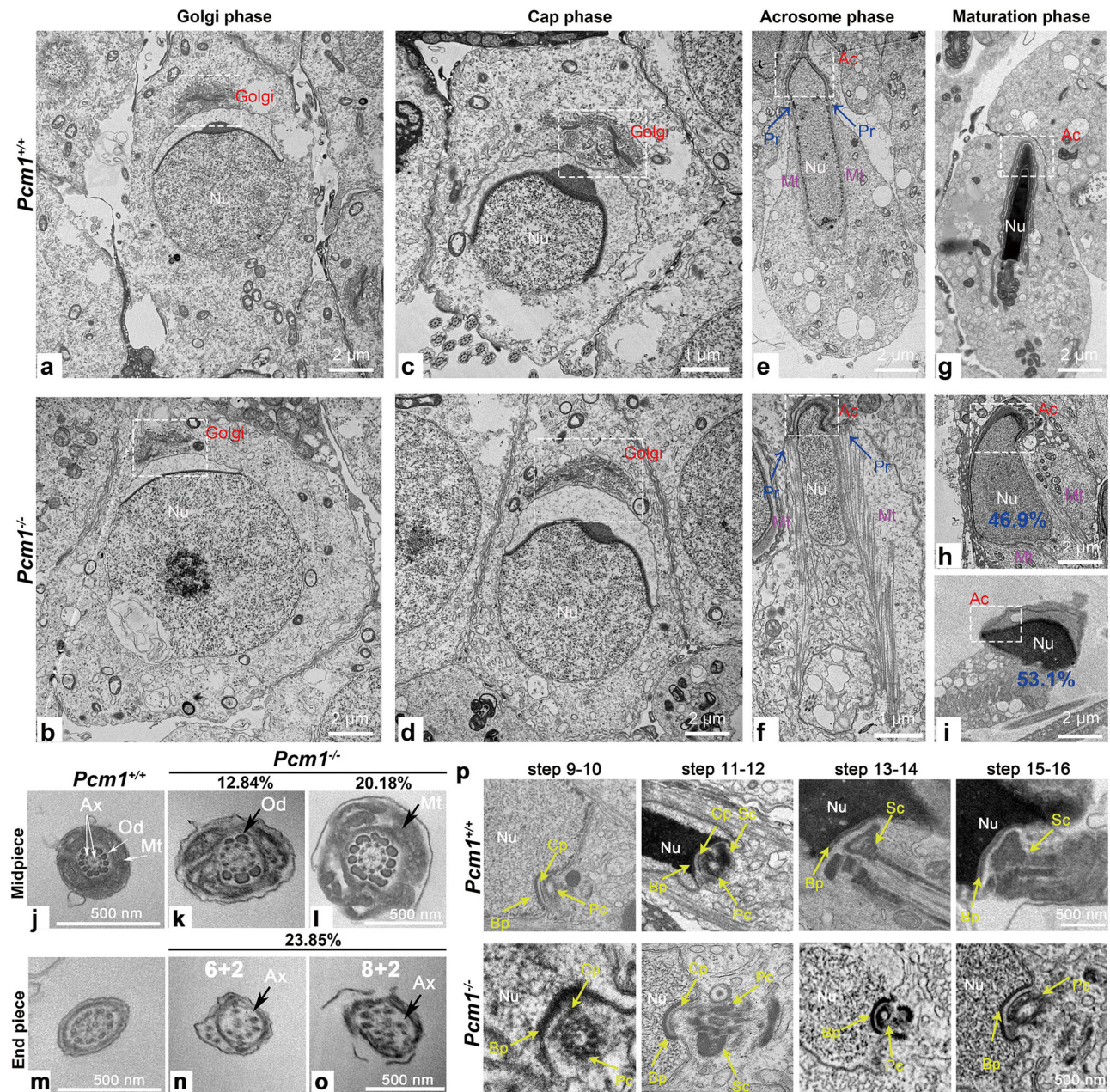
Fig. 4 | Loss of *Pcm1* disrupts spermatid head shaping, neckpiece development and flagellar formation. TEM analyses revealed the process of acrosome biogenesis in the *Pcm1*^{+/+} (**a, c, e, g**) and *Pcm1*^{−/−} (**b, d, f, h, i**) spermatids. Shown were representative images for the Golgi phase (steps 1–3, **a, b**), cap phase (steps 4–7, **c, d**), acrosome phase (steps 8–12, **e, f**) and maturation phase (steps 13–16, **g–i**). Abnormal acrosomal vesicles (**d**), disorganization of manchette (**f, h**) and perinuclear ring (**f**), and irregularly shaped acrosome and head (**f, h, i**) were clearly observed in *Pcm1*^{−/−} mice. Nu nucleus, Ac acrosome, Pr perinuclear ring, Mt manchette. Scale bars: 2 µm (**a, b, e, g–i**), 1 µm (**c, f**). **j–o** TEM analyses revealed the flagellar ultrastructure of the *Pcm1*^{+/+} and *Pcm1*^{−/−} spermatozoa. The *Pcm1*^{+/+}

flagella consists of complete fibrous sheath and typical "9 + 2" arrangement of axonemal microtubules (**j, m**), whereas in the *Pcm1*^{−/−} flagella, the midpiece showed incomplete out dense fibers sheath and mitochondrial sheath (**k, l**), the end piece showed an atypical "6 + 2" or "8 + 2" composition of axonemal microtubules (**n, o**). Ax axoneme, Od out dense fibers sheath, Mt mitochondrial sheath. Scale bars: 500 nm. **p** TEM analyses revealed impaired development of the connecting piece in the *Pcm1*^{−/−} spermatids, showing defective basal plate (Bp), capitulum (Cp), proximal centrioles (Pc) and/or segmented column (Sc). Scale bars: 500 nm. Mice used were 10 weeks old.

axoneme biogenesis[12,16]. PCM1 has been shown to regulate centrosome remodeling during cellular ciliogenesis[28]. To determine whether PCM1 inactivation disturbs centrosome remodeling and disrupts spermiogenesis, the ultrastructure of the neckpiece was ascertained in steps 9–16 spermatids by TEM analysis (Fig. 4p). Abnormal proximal centrioles first appeared at steps 9–10. At steps 11–12, an abnormal basal plate and capitulum were formed, resulting in axoneme initiation in the wrong orientation. By steps 13–14, severe dysplasia of the segmented column

was observed and the capitulum and segmented column were completely disrupted without visible axoneme structures (Fig. 4p). The overall defects in the acrosome, head, manchette, HTCA, and basal body morphology and structure in the *Pcm1*^{−/−} spermatids are also collectively shown in Supplementary Fig. 4a–d. Taken together, these observations confirmed that PCM1 is vital for nuclear condensation and head shaping, HTCA organization, and axoneme biogenesis during sperm maturation.

PCM1 governs the translocation of key proteins for centrosome transition and flagellar formation

To unveil the molecular network by which PCM1 modulates sperm maturation, tandem mass tag (TMT)-based quantitative proteomic analyses were performed with adult $Pcm1^{+/+}$ and $Pcm1^{-/-}$ testes. The DEPs >1.1 or <0.9, with a $p < 0.05$, are regarded as significant upregulated or downregulated, respectively, based on the fold-change ($Pcm1^{-/-}$ vs. $Pcm1^{+/+}$). A total of 8248 proteins were quantified, of which 254 were identified as DEPs (Supplementary Data 1), including 154 downregulated and 100 upregulated proteins. Gene Ontology (GO) annotation and enrichment analyses of the downregulated DEPs in $Pcm1^{-/-}$ testes revealed that the top 20 cellular component GO terms were mainly enriched in spermatid parts, cytoskeleton, centrosome, motile cilium, and manchette (Fig. 5a and Supplementary Data 2). The protein-protein interaction (PPI) network analyses revealed that PCM1 was involved in the processes related to centrosomes, microtubule-based movement, axoneme assembly, and sperm flagellum, as well as the manchette (Supplementary Fig. 5a). In addition, GO annotation plus PPI network analyses suggested that 8 DEPs showed high functional and molecular associations with PCM1 (Fig. 5b and Supplementary Fig. 5b). It is unknown whether and how PCM1 mediates the correct localization and/or function of these proteins during sperm maturation, given the known role of PCM1 in centriolar satellite-mediated transport. A new mechanism likely underlies PCM1 in sperm maturation because motile cilia possess distinct structures not present in immotile cilia and are therefore likely to utilize unique molecular networks.

We hypothesized that PCM1 governs the transport and precise localization of the proteins vital for head shaping and flagella formation to ensure correct sperm maturation. To substantiate this hypothesis, a series of well-controlled and complementary experiments were conducted. First, western blotting showed that the levels of CEP72, CEP131, CCDC39, DRC1, TEKT2, and Ac-tubulin protein were significantly decreased in $Pcm1^{-/-}$ testes (Fig. 5c and Supplementary Fig. 5c). Western blot analyses with differentiating spermatids and mature sperm further confirmed that CEP72, CEP131, CCDC39 and DRC1 were robustly decreased in $Pcm1^{-/-}$ sperm (Supplementary Fig. 5d, e). Second, immunofluorescence in $Pcm1^{+/+}$ testes validated that CEP72, CEP131, CCDC39, and DRC1 were tightly associated with sperm differentiation and/or flagellar formation. All of them were significantly downregulated in $Pcm1^{-/-}$ testes (Fig. 5d and Supplementary Fig. 5f). Third, co-immunoprecipitation and western blot analyses with WT adult testes using an antibody recognizing endogenous PCM1 verified that PCM1 is associated with CEP72, CEP131, CCDC39, DRC1, and Ac-tubulin proteins, but not with tubulin or actin proteins (Fig. 5e). Previous studies have identified PCM1/CEP72 interaction in hTERT-RPE1 cells[32], and PCM1/CEP131 interaction in HEK293 cell[33]. We are the first to verify these interactions in spermatids. Fourth, spermatids in steps 9–14 were separately dissected from $Pcm1^{+/+}$ and $Pcm1^{-/-}$ testes to profile the distribution of these four proteins in a stepwise manner during sperm extension (Fig. 5d). As spermatids differentiate, the centrosome proteins (CEP72 and CEP131) were progressively converted from cytoplasmic dispersion to concentration in the cauda part of the manchette as a dot-like structure closely beneath the head paralleling the transformation of the centrosome. The flagella-related proteins, CCDC39 and DRC1, were progressively cleared or reduced (Fig. 5f). All these dynamic changes were disrupted in $Pcm1^{-/-}$ spermatids. CEP72 and CEP131 proteins were accumulated but quite scattered (Fig. 5f), which indicated defective centrosome reduction. Indeed, co-immunofluorescence of PCM1 and γ-tubulin, a centrosome marker, validated their colocalization during normal spermatid maturation, with γ-tubulin level progressively decreased. However, in $Pcm1^{-/-}$ spermatids, γ-tubulin signal was abnormally retained and exhibited a scattered distribution (Supplementary Fig. 6a). This defective centrosome reduction in the $Pcm1^{-/-}$ spermatids was also validated by co-immunofluorescence of CEP131 and γ-tubulin (Fig. 6a), and immunofluorescence of Centrin1 (Supplementary Fig. 6b, c). These data corroborate that PCM1 is essential for centrosome transition, and represent the molecular changes responsible for defective HTCA structures in $Pcm1^{-/-}$ spermatids (Fig. 4). CCDC39 and

DRC1 also had aberrant cytoplasmic retention (Fig. 5f). It is noteworthy that the tubule network lost the classical zipper-like movement and was extremely elongated at step 14 in $Pcm1^{-/-}$ spermatids, which is consistent with the TEM observations (Fig. 4f) and further corroborates the manchette disorganization in $Pcm1^{-/-}$ spermatids. One important role of the manchette is cargo transporting via intra-manchette transport (IMT). These proteins were likely trapped in the disorganized manchette induced by $Pcm1$ deletion, which prevented the proteins from accurate translocation to promote centrosome transition and/or flagellar formation (Supplementary Fig. 5d, e). As expected, immunofluorescence with epididymal spermatozoa validated that the expression and distribution of the four flagellar proteins were severely disrupted in $Pcm1^{-/-}$ spermatozoa, coincident with defective flagella extension (Supplementary Fig. 5g). These data clearly demonstrated that PCM1 modulates the translocation of centrosomal and flagellar proteins to promote sperm maturation and likely involve manchette-dependent transport.

PCM1 is required for the IMT machinery during spermatid extension

Previous studies have documented that IMT shares features with the intraflagellar transport (IFT) machinery and facilitates nucleocytoplasmic exchange during spermiogenesis[34]. IFT is a highly conserved bidirectional transport mechanism that moves proteins, lipids, and other cargo along microtubules within cilia, therefore vital for the assembly, maintenance, and function of cilia[35]. The mechanism underlying the extension of mammalian sperm flagella is not fully understood but involves IFT-mediated trafficking[36–38]. The above results led us to ask whether $Pcm1$ deficiency interrupts IMT and/or IFT transport with disruption of flagellar extension.

To answer this question, we first examine whether loss of $Pcm1$ alters manchette dynamics. The microtubule plus-end tracking protein EB3, known to regulate manchette assembly[31], exhibited strong expression in $Pcm1^{+/+}$ spermatids at steps 11–12 and then was marked downregulated. EB3 also showed significant colocalization with tubulin. However, its dynamic expression and association with tubulin were severely disrupted in $Pcm1^{-/-}$ spermatids (Fig. 6b). Post-translational modifications of microtubules in the manchette, including acetylation, were proposed to determine IMT events by motors[19,20]. We observed that Ac-Tubulin signals disappeared at step 14 in $Pcm1^{+/+}$ spermatids, paralleling manchette disassembly. However, there was notable retention of Ac-Tubulin signals in $Pcm1^{-/-}$ counterparts (Fig. 6c and Supplementary Fig. 3c). These results supported the previous observations in TEM showing defective manchette assembly and disassembly, a phenotype that was also observed in spermatids lacking $Cep131$[19]. IMT divides up cargo proteins into two locations after the manchette is disassembled: (1) the elongating and condensing spermatid nucleus; and (2) the centrosome and developing sperm tail[34]. PCM1 has been suggested to promote IFT recruitment for cellular ciliogenesis[28]. Costaining with α-tubulin and PNA suggested that the absence of $Pcm1$ interrupted the microtubule-based trafficking for acrosome maturation (Fig. 6d and Supplementary Fig. 3b). Therefore, we explored whether PCM1 is required for IFT recruitment during sperm maturation. IFT81, a subunit of IFT complex B1, and IFT57, a subunit of IFT complex B2, mediate transport of motility-related flagellar cargo. IFT122, a component of IFT complex A, is essential for ciliogenesis[39–42]. It is unknown whether IFT81, IFT57, and IFT122 play a role in flagella extension during spermatid maturation. As anticipated, the IFT81, IFT57, and IFT122 protein levels were significantly declined in $Pcm1^{-/-}$ testes (Supplementary Fig. 6d, e). By dissecting primary spermatids, IFT81, IFT57, and IFT122 were shown to exhibit abnormal local accumulation and de-association with the manchette in steps 9–14 spermatids (Fig. 6e, f and Supplementary Fig. 6f). Eventually, the expression and distribution of IFT81, IFT57, and IFT122 in epidydimal spermatozoa were markedly impaired, accompanied by evident flagellar malformation (Supplementary Fig. 6g).

Kinesin family members (KIFs) are essential molecular motors that play a pivotal role in IFT, KIFs drive anterograde transport, which delivers cargo from the basal body to the ciliary tip, a necessary step for ciliogenesis

a Cellular Component

b

c Pcm1+/+ Pcm1−/−

d Pcm1+/+ Pcm1−/−

e

f
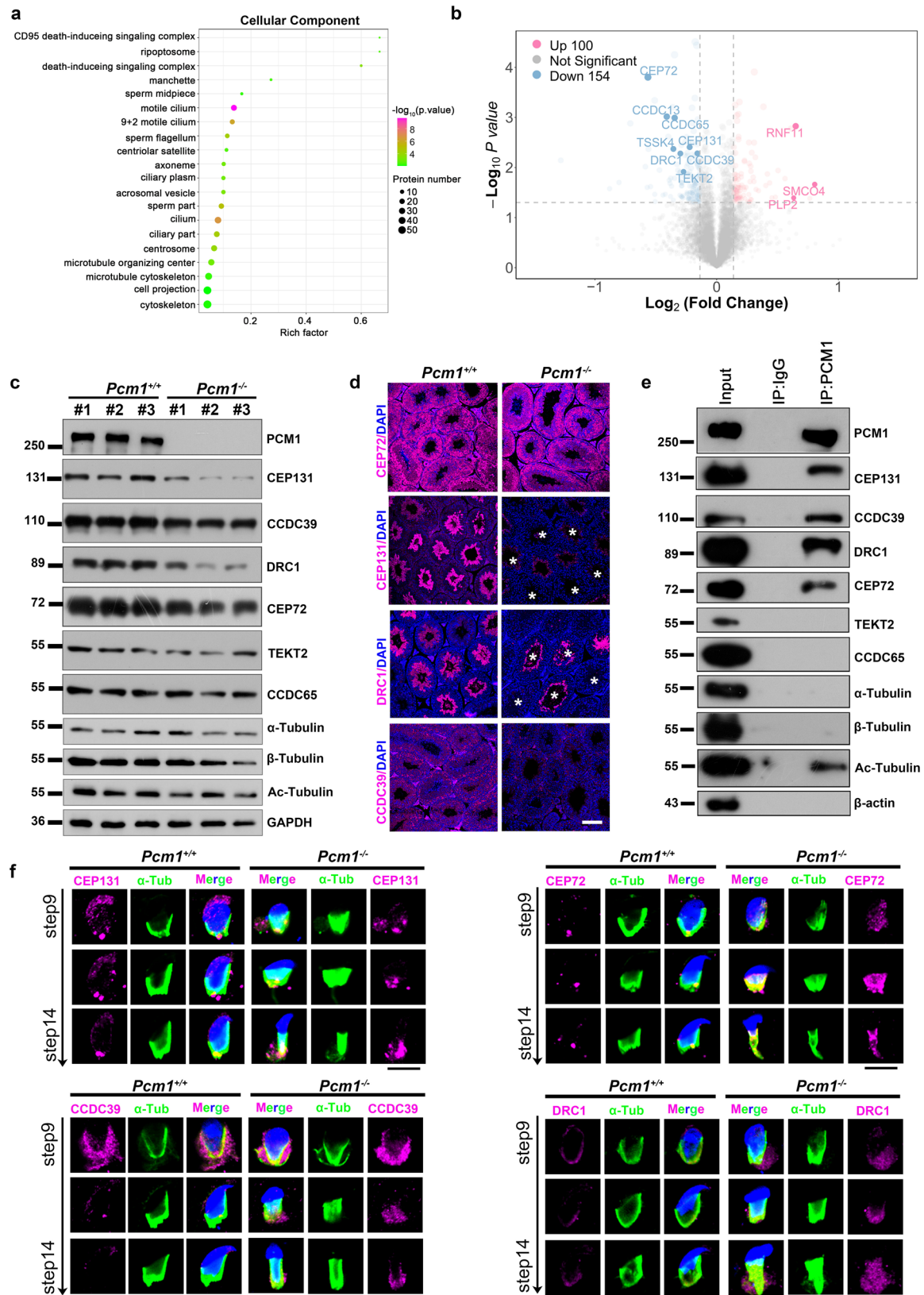
and flagellar formation. In contrast, dyneins are responsible for retrograde transport, which returns cargo to the basal body for recycling[43]. Among the KIF families, Kinesin-2A (KIF2A) is a key molecular motor involved in anterograde transport during IFT. In addition to its role in ciliogenesis, KIF2A localizes to the kinetochore and centrosome during mitosis, where it

regulates the disassembly of the primary cilium, ensuring proper progression of the cell cycle[44–46]. Another important member of the kinesin-2 subfamily is Kinesin-2A-associated protein 3 (KIFAP3), which is essential for the formation and maintenance of protein cargo during IFT along the ciliary axoneme[47]. We found that KIF2A and KIFAP3 exhibited aberrant

Fig. 5 | PCM1 mediates translocation of key proteins for centrosome transition and flagellar formation. a Bubble chart showed top GO terms (cellular component) associated with DEPs in the *Pcm1⁻/⁻* testes identified by TMT proteomic analyses. **b** Volcano plot showing DEPs in the *Pcm1⁻/⁻* mice. Eight important DEPs were highlighted, and their functional associations suggested by PPI analysis was showed in Supplementary Fig. 5b. **c** Western blotting analyses of the testicular protein levels of the DEPs revealed in (**b**). **d** Immunostaining of indicated proteins (magenta) in seminiferous tubules of the *Pcm1⁺/⁺* and *Pcm1⁻/⁻* mice. CEP72 and CCDC39 signals appeared primarily localized in germ cells undergoing meiosis, while CEP131 and DRC1 signals

appeared in elongating spermatids. All of them were decreased in the *Pcm1⁻/⁻* tubules. The asterisks highlight that CEP131 and DRC1 were significantly downregulated in *Pcm1⁻/⁻* seminiferous tubules. Scale bars: 100 μm. **e** Co-IP/WB analyses identified the interactions between PCM1 and indicated proteins in testes. Protein extracts were from the testes of 10-week-old WT mice. **f** Co-immunofluorescence of indicated proteins (CEP72, CEP131, CCDC39 and DRC1, magenta) and α-Tub (green) in dissected spermatids at step 9–14 from the *Pcm1⁺/⁺* and *Pcm1⁻/⁻* mice. Scale bars: 10 μm. Blue indicate nuclei stained with DAPI. Mice used were 10 weeks old.

distribution in *Pcm1⁻/⁻* spermatids (Fig. 6g, h) and spermatozoa (Supplementary Fig. 6g), although the protein levels remained unchanged (Supplementary Fig. 6d, e). Based on the disrupted assembly and disassembly of manchette, we concluded that PCM1 is required for integrity and efficient transport in IMT machinery for proper sperm maturation.

Paternal *Pcm1* deficiency is sufficient to retard embryonic division

To ascertain whether *Pcm1⁻/⁻* sperm heads were functionally capable, the capacity to fertilize eggs by intracytoplasmic sperm injection (ICSI) was determined. A total of 115 and 119 WT eggs were injected with *Pcm1⁺/⁺* and *Pcm1⁻/⁻* sperm heads, respectively. No significant difference existed between the 2 groups in the percentage of fertilized eggs developing into the 2-pronucleus stage (79.31% vs. 82.35%; Fig. 7a, b). However, in the *Pcm1⁻/⁻* group, 47.95% of the 2-pronucleus eggs developed into 2-cell embryos and by the blastocyst stage only 3 blastocysts were obtained (6.38%) in stark contrast to 36 blastocysts (50.70%) in the *Pcm1⁺/⁺* group (Fig. 7a, b). These findings suggested that *Pcm1⁻/⁻* sperm heads with aberrant head differentiation can initiate pronuclear fusion, but induces an arrest of at the 2-cell stage of embryonic division when injected into WT eggs, which is a contributing factor for the sterility of *Pcm1⁻/⁻* males.

Discussion

While the biological functions of PCM1 in cell division and ciliogenesis are well-documented, the role of PCM1 in the reproductive system is unclear. Herein, the role and mechanism of PCM1 in spermatogenesis and embryonic development were elucidated. The key findings are summarized as follows: (1) PCM1 protein levels were significantly decreased in the testes of NOA patients; (2) PCM1 was required for spermatogenesis and spermiogenesis, and PCM1 deficiency led to oligoasthenoteratozoospermia and male factor infertility; (3) the processes throughout sperm maturation, including manchette organization and HTCA formation, nuclear condensation and head shaping, and particularly flagellogenesis, were extensively disrupted upon PCM1 dysfunction; (4) PCM1 governed the accurate positioning of centrosomal proteins, such as CEP72 and CEP131, and of flagellar proteins, such as DRC1 and CCDC39, likely through the IMT, to facilitate proper centrosome remodeling and axoneme biogenesis (Fig. 8, intramanchette transport); and (5) the *Pcm1⁻/⁻* sperm heads failed to promote embryonic division when injected into WT oocytes by ICSI. Thus, the current study established a novel function and mechanism underlying PCM1 in regulating spermatogenesis and spermiogenesis, which advanced our understanding of centrosome-related proteins in sperm maturation and embryonic development (Fig. 8).

To date, the molecular mechanism underlying sperm tail assembly and prevention of separation from the heads during vigorous beats remains unclear. *Pcm1⁻/⁻* males exhibited an extremely high rate of round sperm (66%), indicating that loss of *Pcm1* principally disrupted flagellar biogenesis. It has been proposed that the manchette microtubules are essential for targeting structural and functional molecules necessary for nuclear shaping and sperm tail development[47]. Our findings further highlight the role of the manchette in sperm extension because disorganized manchette were notably observed in the elongating spermatids lacking *Pcm1*, which is responsible for the observed cylindrical nucleus, defective nuclear condensation, and malformed acrosome. The question is how PCM1 regulates manchette organization. Because PCM1 is required for microtubule

organization during mitosis[48], it is reasonable to infer that PCM1 also governs microtubule organization of the manchette during spermatid extension. However, our co-IP experiments failed to detect interactions between PCM1 and tubulin or actin. It is possible that associations exist but were rapidly changing or sensitive to the immunoprecipitation experimental conditions. However, PCM1 precipitated large amounts of Ac-tubulin, indicating that PCM1 may associate with steady microtubules for transporting cargo.

Another possible cause for a defective manchette might be impaired centrosome integrity owing to PCM1 inactivation given that the centrosome is postulated to serve as the nucleation site for manchette microtubules[31]. PPI analysis with the proteomic data suggested 8 DEPs that tightly associate with centrosome and flagellum were significantly downregulated in KO testes, of which CEP72 and CEP131 are known centriolar satellite proteins and interacts with PCM1[32,33]. CEP131 is required for sperm maturation and male fertility[19,28]. Notably, deletion of *Cep131* in mice disrupts manchette organization, HTCA structure and spermatids nuclear shaping[32], quite resembling the phenotypes in *Pcm1*-KO mice. CEP72 coordinates with PCM1 and CEP290 to recruit Bardet-Biedl Syndrome (BBS) proteins to the cilium in RPE1 cells[34]. It has recently been shown that deletion of *Cep72* does not affect the viability and fertility of mice but results in sperm with incomplete flagellum structures[49]. Moreover, a *DRC1* gene mutation has been identified in male patients with fertility defects, and deletion of *Drc1* in mice leads to multiple morphologic abnormalities of the sperm flagella and male factor infertility[50]. CCDC39 and CCDC65 are required for sperm flagella structure in humans[39–41]. Downregulation of TEKT2 is also associated with male factor infertility[42]. TSSK4 has a role in the structural integrity of sperm flagella[51,52]. These reports suggest the role of PCM1 in centrosome remodeling and flagellar formation. Our observations support the notion that impaired centrosome remodeling disrupts manchette dynamics, as the four important centrosome- or satellite-associated proteins, CEP131, CEP72, CCDC39 and DRC1 have molecular interactions with PCM1, and are quite dispersed in cytoplasm and lost association with tubulin system following deletion of *Pcm1*. TEM analyses revealed striking impairments in the connecting piece structures, including the capitulum and segmented column, which have been suggested to arise from the "pericentriolar material"[53]. In addition to perturbing microtubule assembly, loss of *Pcm1* also caused delay in manchette removal, possibly involving dysfunction of the microtubule severing complex or ubiquitin-mediated protein degradation. Therefore, PCM1 serves as a cargo transporter that recruits essential components for centrosome remodeling and timely microtubule formation and clearance, thereby disrupting manchette dynamics and importantly, flagellogenesis, in the event of PCM1 inactivation. Consistently, the centrosome/flagellum-associated proteins discussed above (CEP131, CEP72, CCDC39, DRC1) also showed notable reduction in the KO testes.

In many mouse models with mutations in IFT or microtubule-related proteins, the manchette is abnormally elongated, causing the nucleus to deform into a cylindrical shape along the elongated manchette[31,54]. These phenotypes highly resemble what we observed in *Pcm1⁻/⁻* males. Our proteomic analyses revealed that the downregulated DEPs in *Pcm1⁻/⁻* testes were primarily linked to microtubules-based movement, cilium organization, and spermatid differentiation, all closely relevant to IMT. The IMT machinery greatly resembles IFT. Therefore, we hypothesized that PCM1 is not only required for manchette dynamics but also for protein transport in IMT. Evidence supporting this notion was derived from the observation that
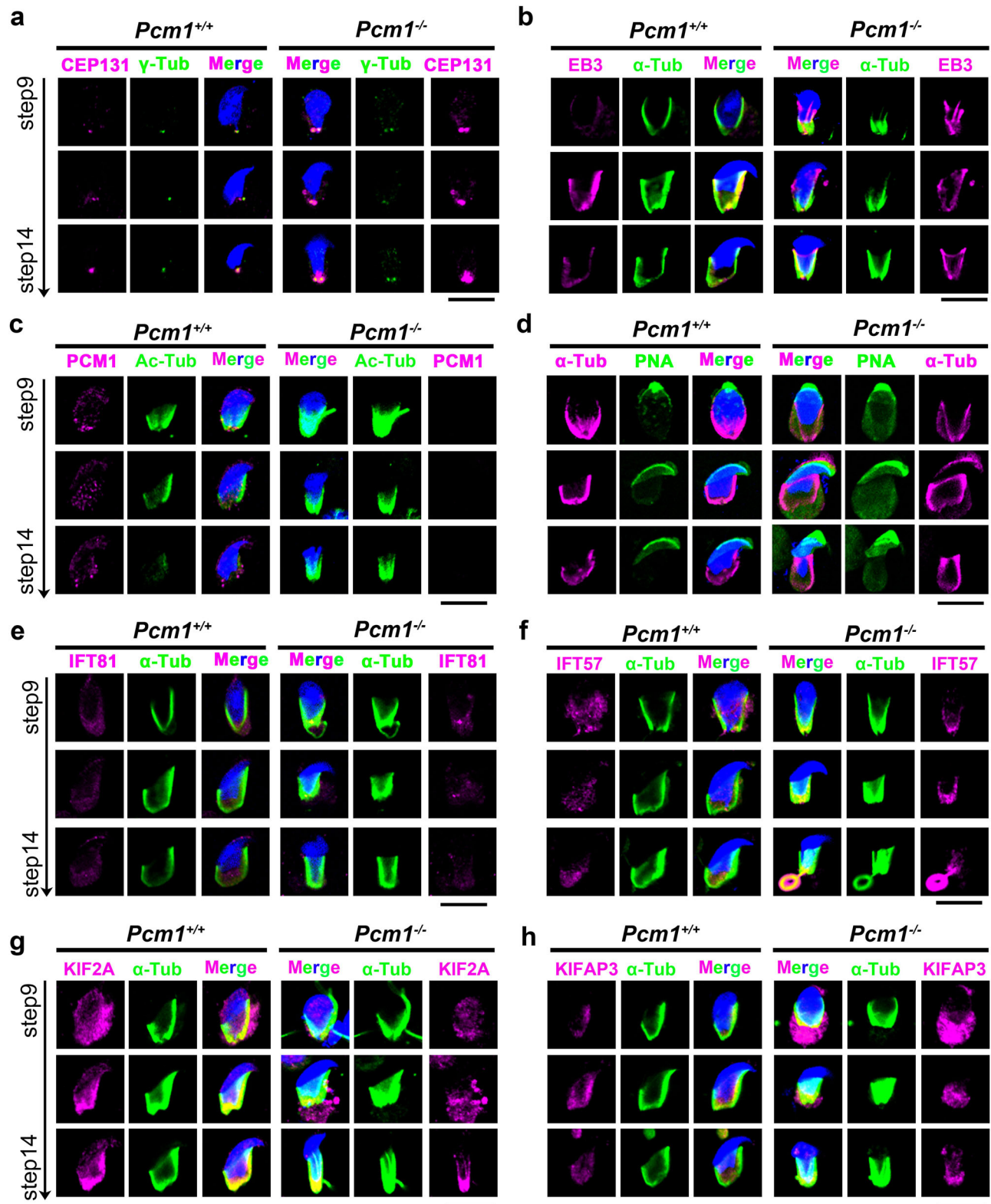
Fig. 6 | PCM1 is required for intramanchette transport machinery during spermatid extension. a Co-immunofluorescence of CEP131 (magenta) and γ-Tub (green, a centrosome marker) in step 9–14 spermatids of the *Pcm1*+/+ and *Pcm1*−/− mice. **b** Co-immunofluorescence of EB3 (magenta, a manchette marker) and α-Tub (green) in step 9–14 spermatids of the *Pcm1*+/+ and *Pcm1*−/− mice. **c** Co-immunofluorescence of PMC1 (magenta) and Ac-Tub (green, labeling steady microtubules in manchette) in step 9–14 spermatids of the *Pcm1*+/+ and *Pcm1*−/− mice. **d** Co-immunofluorescence of α-Tub (magenta, labeling manchette) and PNA (green, labeling acrosome) in step 9–14 spermatids of the *Pcm1*+/+ and *Pcm1*−/− mice. **e, f** Co-immunofluorescence of α-Tub (green) and IFT proteins (magenta, IFT81, IFT57) in step 9–14 spermatids of *Pcm1*+/+ and *Pcm1*−/− mice. **g, h** Co-immunofluorescence of α-Tub (green) and KIF proteins (magenta, KIF2A, KIFAP3) in step 9–14 spermatids of *Pcm1*+/+ and *Pcm1*−/− mice. All scale bars: 10 μm. Blue indicate nuclei stained with DAPI. Mice used were 10 weeks old.
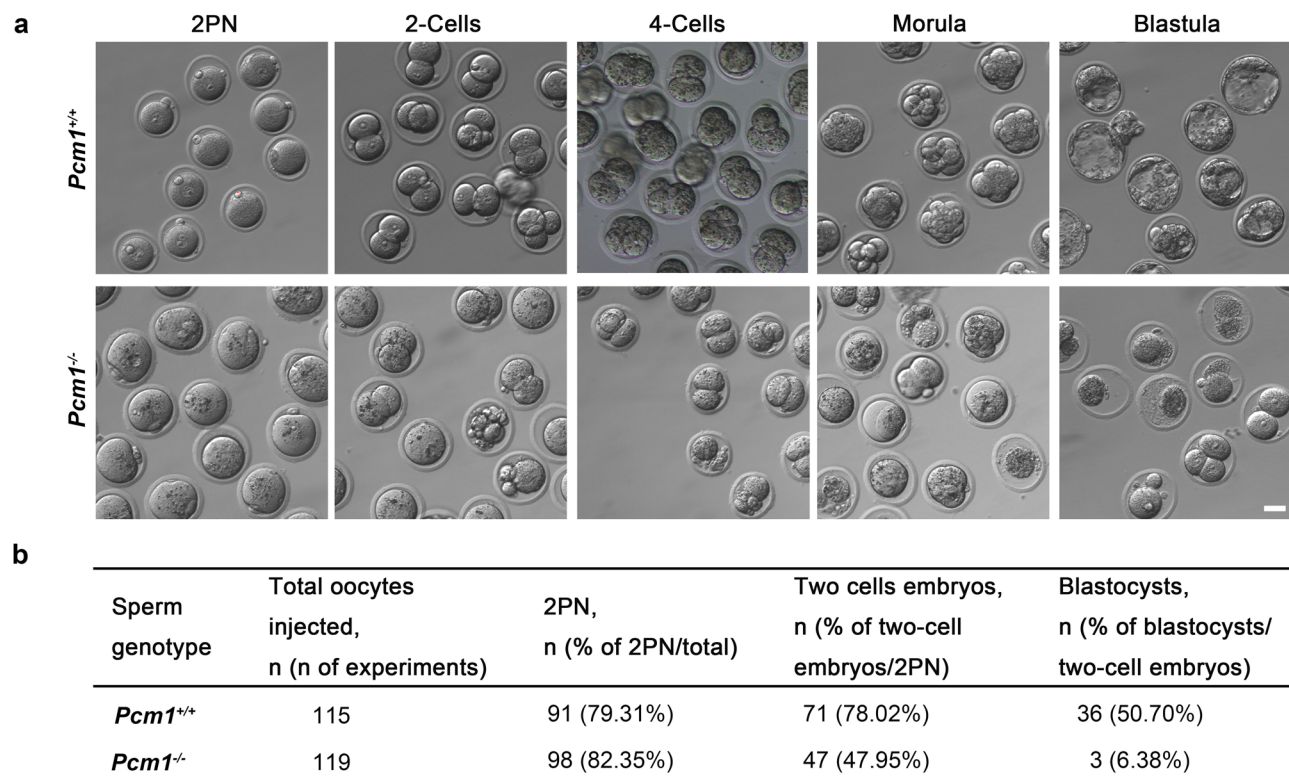
Fig. 7 | Paternal PCM1 is indispensable for embryo development. a Representative images showed the developmental process of embryos from WT oocytes injected with the *Pcm1*^{+/+} or *Pcm1*^{−/−} sperm heads via ICSI. **b** Table chart illustrated the data in (**a**). A total of 115 and 119 WT oocytes were injected with *Pcm1*^{+/+} and *Pcm1*^{−/−} sperm heads, respectively, and they generated comparable 2-pronucleus eggs. Severe embryonic division retardation in the *Pcm1*^{−/−} group was first seen at 2-cell stage.

Sperm genotype	Total oocytes injected, n (n of experiments)	2PN, n (% of 2PN/total)	Two cells embryos, n (% of two-cell embryos/2PN)	Blastocysts, n (% of blastocysts/ two-cell embryos)
Pcm1^{+/+}	115	91 (79.31%)	71 (78.02%)	36 (50.70%)
Pcm1^{−/−}	119	98 (82.35%)	47 (47.95%)	3 (6.38%)

Fig. 8 | Working model depicts how PCM1 regulates spermiogenesis and embryo development. During spermatid elongation, PCM1 governs the correct transport of centrosomal proteins (e.g. CEP72 and CEP131) and flagellar proteins (e.g. CCDC39 and DRC1), in an IMT-dependent manner, to facilitate centrosome remodeling and flagellogenesis (enlarged intramanchette transport square), thus ensuring proper sperm maturation and embryo development. PCM1 dysfunction disrupts the expression and transition of these important structure proteins and impairs sperm maturation. Such defects in paternal centrosome integrity consequently lead to embryonic developmental arrest, even when ICSI is applied to bypass fertilization barrier. These findings establish a functional continuum between spermiogenesis and embryogenesis, wherein germ cell centrosome homeostasis exerts latent influence on post-fertilization development. This figure was originally created by the authors using Adobe Illustrator. The elements of round spermatid and HTCA were referenced from Wang et al.[62] and Shen et al.[16], respectively.
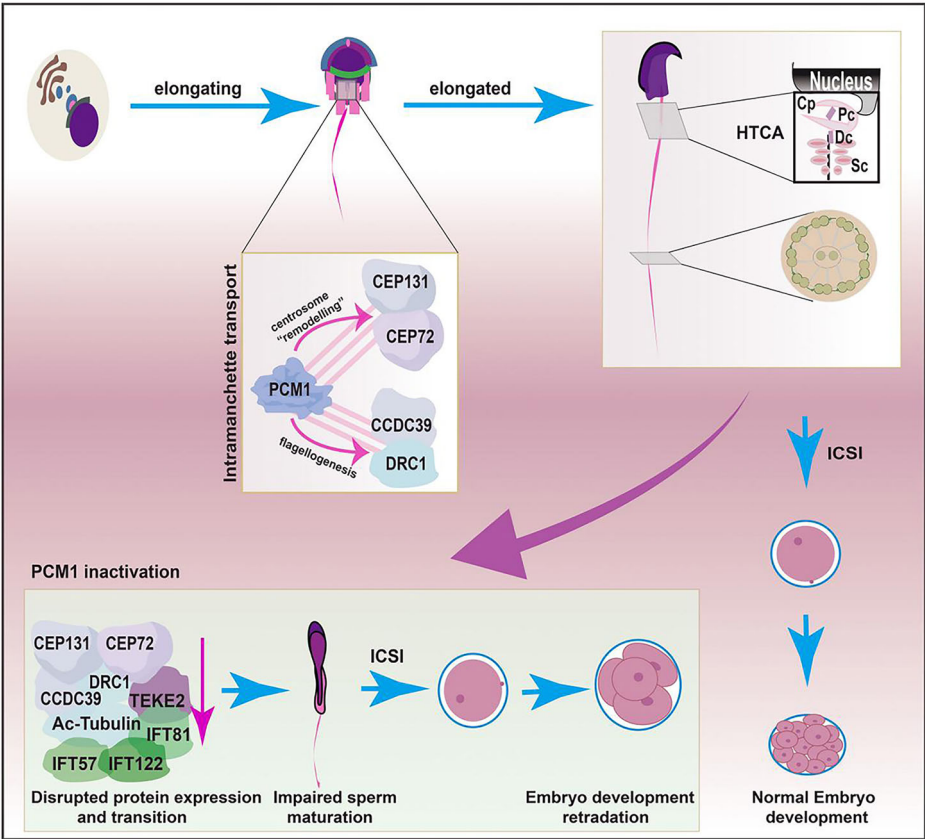
the IFT proteins, such as IFT57, IFT81, IFT122, KIF2A, and KIFAP3, exhibited strong associations with tubulin and transition from cytoplasmic dispersal to accumulation at the caudal site of the manchette during sperm extension, which were extensively disrupted following *Pcm1* deletion. Furthermore, the expression and distribution of IFT proteins were disturbed in *Pcm1*−/− spermatozoa, further leading to compromised sperm motility. Taken together, we hypothesized that structural proteins of the sperm tail are transported through IMT to the basal body at the base of the developing sperm tail and via IFT to the construction site in the flagellum, wherein PCM1 has a central role. Thus, sperm head shaping and tail formation are extensively disrupted upon PCM1 dysfunction.

We observed that injection of *Pcm1*−/− sperm heads into WT oocytes via ICSI failed to overcome reproductive defects, which showed severe arrest of development after the 2-cell stage. Zygote genome activation (ZGA) in mice initiates during the late 1-cell to early 2-cell stage[55]. We speculated that genetic alterations resulting from *Pcm1* deletion, characterized by incomplete nuclear condensation and chromatin remodeling, probably disrupt zygote genome activation, thereby causing division retardation. *Pcm1*+/+ and *Pcm1*−/− sperm heads generated a comparable number of 2-pronuclus embryos, consistent with the widely accepted notion that the murine sperm centrosome is dispensable for aster formation to facilitate pronuclear fusion, which is a process facilitated by multiple aster formation in the oocyte[56]. However, *Pcm1*−/− females had complete reproductive capacity (data not shown), suggesting that PCM1 is unnecessary for oogenesis or oocyte microtubule organization during aster formation and subsequent embryonic development. These findings suggest that the paternal PCM1, but not the maternal PCM1, is indispensable for germ cell differentiation. Moreover, the sperm null for PCM1 cannot support embryonic development, highlighting the contribution of paternal factors to fertility.

In conclusion, our work expands the current understanding of the role of PCM1 in spermatogenesis and spermiogenesis. We also elucidated how PCM1 governs the precise transition of centrosomal proteins (e.g., CEP72 and CEP131) and flagellar components (e.g., DRC1 and CCDC65) via IMT to ensure proper sperm maturation. Of particular concern is the profound embryo development retardation, even via ICSI injection of *Pcm1*−/− sperm heads into WT oocytes, highlighting the comprehensive role of paternal factors, particularly the centrosomal proteins, in fertilization, embryonic development, and reproduction. Based on these findings we suggest *PCM1* as a novel candidate gene implicated in human infertility. The factors that cause PCM1 dysfunction and whether there are potential *PCM1* mutations implicated in human infertility are unknown. Further in-depth investigations focusing on the mechanism underlying PCM1 in spermatogenesis, spermiogenesis, fertilization, and embryo development would greatly advance the development of preventive and therapeutic strategies for reproductive defects in human.

Methods

Inclusion of clinical patients and testicular biopsy collection

Clinical patients with NOA, characterized by severe spermatogenic arrest and no testicular spermatids and epididymal sperm, were identified by visual microscopy and a computer-assisted semen analysis (CASA), in combination with a testis biopsy for testicular histology examination. Patients with OA (normal spermatogenesis, tubular lumen obstruction) were used as controls. Patients with the following characteristics were excluded: (1) a history of testicular surgery or injury, cryptorchidism, genital tract infection, positive anti-sperm antibody, etc; (2) severe chronic or acute diseases, including those of the cardiovascular, cerebrovascular, hepatorenal, or blood system; (3) ejaculatory dysfunction, including non- or retrograde ejaculation; and (4) karyotype anomalies or azoospermia factor (AZF) microdeletions. The age range for patients was 20–39 years and the median age for the NOA group was 31 and that for the OA group was 30. The Third Affiliated Hospital Ethics Committee of Guangzhou Medical University approved the experiments involving human subjects (2017-055). The relevant research has obtained informed consent from all participating patients. All ethical regulations relevant to human research participants were followed.

Proteomics analyses

Three testis biopsy samples from each group were subjected to isobaric tags for relative and absolute quantification (iTRAQ) analysis (conducted by Fitgene Biotech Company, Guangzhou, China), for the screening of differentially expressed proteins, as described in our previous report[57,58]. Briefly, the frozen testes were grinded by liquid nitrogen and then lysed in 500 μl of SDS lysis buffer (Add 1× PMSF before use) containing 7 M Urea, 2 M Thiourea, 20 mM Tris base and 0.2% SDS. Then the samples were sonicated and centrifuged to collect the supernatant. Protein concentration was estimated by the Bradford method. Then, proteins were digested with trypsin (Promega, USA) at 37 °C at a ratio of 1:50 (enzyme-to-substrate) overnight. Each sample was labeled separately with two of the eight available tags (OA: 114 and 116 tags; NOA: 117 and 119 tags) (Applied Biosystems, Sciex). All labeled peptides were pooled together. The Ultimate 3000 HPLC system (Dionex, USA) equipped with a 2.00-mm-inner-diameter *100-mm-long Gemini-NX 3 u C18110Acolumns (Phenomenex, USA) was used for High-pH fractionation. The iTRAQ-tagged peptides fractionation was performed using a linear binary gradient from 15 to 50% B (20 mM HCOONH 4, 2 M NaOH, 80% ACN) (pH 10) at 0.2 ml/min for more than 45 min. The fraction was resuspended in loading buffer (0.1% FA,2% ACN) and separated with an Ultimate 3000 nano-LC system equipped with a C18 reverse phase column (100-μm inner diameter, 10-cm long, 3-μm resin from Michrom Bioresources, Auburn, CA). Then, the LC eluent was subject to Q Exactive (Thermo Fisher) in an information-dependent acquisition mode. MS spectra were acquired across the mass range of 400–1250 m/z in high resolution mode (>30,000) using 250 ms accumulation time per spectrum. Tandem mass spectra were recorded in high sensitivity mode (resolution >15,000) with rolling collision energy on and iTRAQ reagent collision energy adjustment on.

Tandem mass tag (TMT)-based quantitative proteomic analysis with the testes from the *Pcm1*+/+ and *Pcm1*−/− males (n = 3, 10 weeks old) were performed by Shanghai Applied Protein Technology Co., Ltd. Briefly, testes were first lysed with SDT buffer (4% (w/v) SDS, 100 mM Tris/HCl (pH 7.6), 0.1 M DTT) and trypsinized with the filter-aided proteome preparation (FASP) technique. Then, 100 μg of extracted peptide was used for TMT labeling using TMT 6/10 plex Isobaric Label Reagent (ThermoFisher Scientific, Shanghai, China) according to the manufacturer's instructions. A Pierce High pH Reversed-Phase Fractionation Kit (ThermoFisher Scientific) was used to fractionate samples of the TMT-labeled digests into 10 fractions via step gradient elution with increasing concentrations of acetonitrile according to the instructions. Each fraction was injected for nano-liquid chromatography-tandem mass spectrometry (nanoLC-MS/MS) analysis, and MS analysis was then conducted using a Q-Exactive mass spectrometer. The raw data for the MS analysis were written to RAW files, and we used Mascot 2.2 and Proteome Discoverer 1.4 software for library identification and quantification. Finally, bioinformatic analyses, including Gene Ontology (GO) enrichment and Kyoto Encyclopedia of Genes and Genomes (KEGG) pathway analyses, were conducted.

Tissue microarray, immunohistochemistry and expression ranking

Thirty NOA and 25 OA testis biopsy samples were subjected to tissue microarray processing by Shanghai Bio-chip Biotechnology (Shanghai, China) and sectioned. Immunohistochemistry (IHC) staining was performed on a 5-μm section with an anti-PCM1 antibody (Supplementary Table 4) and a horseradish peroxidase (HRP)-conjugated anti-IgG secondary antibody (111-035-003; Jackson Immunoresearch, West Grove, PA, USA), and was visualized with diaminobenzidine. Hematoxylin was used as a counterstain on the slides. Images were obtained by Axio Scope A1 microscope (Carl Zeiss Microscopy GmbH, Jena, Germany) and analyzed by using AxioCam HRc3 S/N 2254-ZEN 2011 software. The staining extent and intensity were estimated to determine the expression level. The staining intensity was scored as 0 (achromatic color), 1 (pallide flavens), 2 (deep yellow), or 3 (brown). The staining extent was scored as 0 (<5%), 1 (5–25%), 2 (26–50%), 3 (51–75%), or 4 (>75%), according to the percentages of

positively stained areas in relation to entire sample areas. The final staining score (0–8) was calculated by adding the staining intensity and extent scores. For statistical analysis, samples having a final staining score of 0 were deemed negative (−), 1–2 were mildly positive (+), 3–5 were moderately positive (++), and 6–8 were strongly positive (+++).

Animals, husbandry and genotyping

The *Pcm1* knockout mice (*Pcm1*[em17Gpt], Strain NO. T016698) of C57BL/6J background were purchased from GemPharmatech (Nanjing, Jiangsu, China), in which the exons 3–6 of *Pcm1*-201 transcript (ENSMUST00000045218.9) were deleted via the CRISPR/Cas9 technology (Supplementary Data 4). Homozygous male *Pcm1*^{−/−} (KO) mice were generated by mating heterogeneous male and female *Pcm1*^{+/−} mice, and the male WT (*Pcm1*^{+/+}, WT) littermates were used as controls. DNA isolated from tail biopsies was used to genotype the mice via PCR in combination with agarose gel electrophoresis. The primer sequences for genotyping were listed in Supplementary Table 5. For the primer pair F1/R1, the PCR product of 11,289 bp represents the WT band, and the product of 333 bp represents the KO band, and because the WT band is too large, we hardly detected a WT band. For the primer pair F2/R2, the PCR product of 412 bp represents the WT band, and no product for KO band, and both bands were detected in heterozygote mice.

Mice were housed at controlled temperatures of $25 \pm 1\,°C$, on a 12-h light/12-h dark cycle, with lights on from 06:00–18:00. Standard rodent chow and water were provided ad libitum throughout the study period. Mice were euthanized by CO_2 asphyxiation or alternatively with sodium pentobarbital anesthesia overdose followed by cervical dislocation. Testes were collected immediately post-mortem for analysis. All animal experiments were approved by the Ethical Committee for Animal Research of Southern Medical University (ethical review number L2019176), and conducted according to the Committee's guidance. We have complied with all relevant ethical regulations for animal use.

Histomorphological examination

Mice were sacrificed via cervical dislocation, the testes and epididymides were removed and weighed, fixed in modified Davidson's fixative for 24–48 h, followed by 70% ethanol rinsing. Tissues were dehydrated in graded ethanol, cleared in xylene, infiltrated with paraffin wax and embedded in oriented blocks. Sections were deparaffinized and dehydrated through a graded ethanol series, and then rehydrated by descending concentrations of ethanol. At least three sections from each testis and epididymis (5 μm, taken 100 μm apart) were stained with hematoxylin and eosin (H&E) for regular histological examination.

Periodic acid-Schiff (PAS) staining was performed on testicular sections, which were stained with a PAS dye solution (G1280, Solarbio, Beijing, China), for the assessment of seminiferous tubule development and spermatogenic stage. Images were taken with an Axio Scope A1 microscope.

Immunofluorescence

For the immunostaining of testicular tissues, samples were first fixed with 4% formaldehyde in PBS. After subsequent dehydration with an ethanol gradient, tissues were embedded in paraffin and sectioned into 3-μm sections, and then deparaffinized and dehydrated through a graded ethanol series. The sections were repaired in citrate buffer under high pressure for 5 min, followed by 5 min in PBS, and incubated with 5% BSA for 1 h. After incubation with primary antibodies (listed in Supplementary Table 4) and Alexa-Fluor-488-or Alexa-Fluor-594-labeled secondary antibodies (Jackson Immunoresearch), nuclei were stained with 4, 6-diamidino-2-phenylindole DAPI (D9542, Sigma-Aldrich, Shanghai, China).

For the immunostaining of germ cells, cells were fixed with 4% formaldehyde in PBS for 10 min, permeabilized with 0.2% Triton X-100 (T9284, Sigma-Aldrich) for 15 min, and blocked with 5% BSA for 1 h at 25 °C. Next, the cells were incubated with primary antibodies overnight at 4 °C, followed by 1 h of incubation with AlexaFluor-488-or Alexa-Fluor-

594-labeled secondary antibodies at room temperature. Nuclei were counterstained with DAPI.

Images were obtained using a confocal laser scanning microscope (Olympus FV10, Tokyo, Japan), equipped with a Hamamatsu camera. Red filters (range 575–615 nm) and green filters (range 500–550 nm) were used for Alexa 594 and Alexa 488 staining, respectively. Images were then processed using FV10-ASW 3.1 software (Olympus), and the intensity of positive signals was analyzed using the Image J software (1.53t, National Institutes of Health, USA).

Cell apoptosis assay

Cell apoptosis was evaluated in testicular sections by the terminal deoxynucleotidyl transferase-mediated dUTP nick end-labeling (TUNEL) assay, using the DeadEnd Fluorometric TUNEL System (G3250, Promega, Madison, WI, USA) to visualize DNA fragmentation in situ. At least three sections from each testis (3 μm, taken 100 μm apart) were stained. Images were taken with a FluoView FV1000 confocal microscope, and TUNEL-positive signals in each section were counted.

Sperm concentration, motility and morphology assessments

Sperm were collected from shredded unilateral caudal epididymis, and maintained in 500 μL M2 medium (M7167, Sigma-Aldrich) supplemented with 3% bovine serum albumin (BSA, A1933, Sigma-Aldrich) at 37 °C for 15 min. The sperm concentration and motility were assessed using microscopy and a CASA (Hamilton Thorne Inc., Beverly, MA, USA) under parameters for mouse (Supplementary Table 6). Video recordings of sperm were obtained using a Nikon NT-88V3 inverted microscope (Nikon Instruments, Tokyo, Japan). Morphological examination was performed on smeared sperm, and the abnormalities in head, neck or tail were classified and recorded.

Isolation of individual spermatids

Individual spermatids were isolated following the protocol from a previous report[59]. In brief, testes were decapsulated and placed in 5 mL DMEM/F12 containing 0.5 mg/mL collagenase IV and 1.0 mg/mL DNase I (both from Sigma-Aldrich) in shaking water bath at 33 °C for 30 min, then centrifuged for 5 min at 1000 rpm, and filtered with 70 μm and 40 μm nylon filters (Corning, NY, USA). The mixed testicular cells were fixed in 4% paraformaldehyde/PBS (containing 4% sucrose) at room temperature for 15 min, and then washed three times with PBS. Following staining with DAPI and examination with FV10-ASW 3.1 software (Olympus) to assess the purity, the obtained testicular cells were used for immunofluorescent staining.

Protein extraction and western blotting

Tissues or cells were lysed in RIPA buffer containing 50 mM Tris-HCl pH 8, 150 mM NaCl, 1% Triton X-100, 0.1% sodium deoxycholate, 0.1% sodium dodecyl sulfate (SDS), and 1× protease inhibitor cocktail (P1046, Beyotime Biotechnology, Shanghai, China). After centrifugation at $12,000 \times g$ at 4 °C, the supernatant was collected and the protein concentration was quantified by a BCA kit (C503021, Sangon Biotech, Shanghai, China), and finally boiled in 2× SDS loading buffer. Thirty microgram of protein was then subjected to 6–15% SDS-polyacrylamide gel electrophoresis (PAGE) and electrotransferred to nitrocellulose membranes (10600001, GE Healthcare Life Sciences, Beijing, China). The membranes were then blocked in 5% nonfat dry milk for 1 h at room temperature, washed, and incubated with primary antibodies (Supplementary Table 4) at 4 °C overnight. The membranes were further washed, incubated with HRP-conjugated secondary antibody (Jackson Immunoresearch) for 1 h at room temperature, washed again, and finally visualized using an enhanced chemiluminescence kit (NEL105001EA, PerkinElmer, Waltham, MA, USA). Quantification was performed by measuring the gray value of bands using the Image J software.

Co-immunoprecipitation

Testicular tissues were homogenized in CHAPS-containing lysis buffer [0.3% CHAPS, 40 mM HEPES (pH 7.4), 150 mM NaCl, 2 mM

Article

ethylenediamindium pyrophosphate, 10 mM sodium glycerophosphate, 50 mM NaF, plus protease inhibitors] at 4 °C for 20 min, centrifuged at 12,000 × g at 4°C for 10 min, and the supernatant were collected and incubated with an anti-PCM1 primary antibody at 4 °C for 2 h with continuous rotation. A 50% slurry of protein A/G Sepharose (100 μl, Cytiva, Uppsala, Sweden) was then added and incubated for an additional 1 h. The beads were washed with CHAPS-containing lysis buffer, eluted with 2× SDS loading buffer, and boiled for 10 min at 100 °C. Immunoprecipitated proteins were resolved by SDS-PAGE, and finally analyzed by immunoblotting.

Electron microscopy
For scanning electron microscopy (SEM), spermatozoa were preserved on slides by applying 2.5% glutaraldehyde, and refrigerated overnight at 4 °C. After rinsing with 1× PBS buffer three times, spermatozoa were dehydrated using an ethanol gradient (30, 50, 75, 95, and 100% ethanol), and dried using a CO₂ critical-point dryer. After metal spraying with an ionic sprayer meter (Eiko E-1020, Hitachi, Japan), the samples were observed and images were captured by a scanning electron microscope (S-3000N, Hitachi, Japan).

For transmission electron microscopy (TEM), samples were fixed routinely with 3% glutaraldehyde and osmium tetroxide. Samples were then post-fixed with 1% OsO_4 and sucrose and dried using ethanol concentrations that were gradually increased. The samples were then inserted into Epon 812. Uranyl acetate and lead citrate were used to stain ultrathin slices, which were subsequently examined using a transmission electron microscope (H-7500, Hitachi, Japan) that had an 60 kV accelerating voltage.

Intracytoplasmic sperm injection
Intracytoplasmic sperm injection (ICSI) was performed using standard techniques as previously described[60,61]. Briefly, female KM mice (purchased from Animal Center of Southern Medical University) were first injected with 5 IU of pregnant mare serum gonadotropin (PMSG, Ningbo Second Hormone Factory, Zhejiang, China). Forty-eight hours later, the female mice were injected with 5 IU of human chorionic gonadotropin (hCG, Ningbo Second Hormone Factory). MII-arrested oocytes were collected from the ampulla of fallopian tube and incubated in M2 medium at 37.5 °C in an incubator with 5% CO_2. Spermatozoa collected from cauda epididymides were incubated in M2 medium, and detached sperm heads were injected into MII oocytes with a Piezo-driven pipette, followed by culture in KSOM medium (MR-020P-D, Millipore) in 5% CO_2 at 37 °C. The injected oocytes were analyzed 5–8 h after ICSI and the embryonic development was assessed and photographed every day after ICSI.

Statistical analysis and reproducibility
All experiments were performed in triplicate. Data are presented as mean values ± standard deviation (SD). The differences in PCM1 expression in the tissue microarray between OA and NOA groups were analyzed using the Wilcoxon signed-rank test (SPSS 13.0; SPSS, Chicago, IL, USA). Other data were analyzed by GraphPad Prism 8.0 software (GraphPad Prism, San Diego, CA, USA), using two-tailed *t*-test for two groups, or one-way analysis of variance with multiple comparisons, followed by the Bonferroni post hoc test for significance. $p < 0.05$ was considered statistically significant.

Data availability
Data are available from the corresponding author on reasonable request. Uncropped blots and gels for all the experiments presented in the manuscript can be found in Supplementary Fig. S7. The source data for all statistical graphs are provided in Supplementary Data 3. The mass spectrometry proteomics data for NOA and OA testicular biopsy have been deposited in the ProteomeXchange Consortium via the PRIDE partner repository with the dataset identifier PXD060811. The proteomics data for *Pcm1*-KO and WT mice have been deposited to the ProteomeXchange Consortium (http://proteomecentral.proteomexchange.org) via the iProX partner repository with the data set identifier PXD051164. Other data are available upon reasonable request.

References
1. Fainberg, J. & Kashanian, J. A. Recent advances in understanding and managing male infertility. *F1000Res* **8**, F1000 Faculty Rev-670 (2019).
2. Dyer, S. J. International estimates on infertility prevalence and treatment seeking: potential need and demand for medical care. *Hum. Reprod.* **24**, 2379–2380 (2009).
3. Eisenberg, M. L. et al. Male infertility. *Nat. Rev. Dis. Prim.* **9**, 49 (2023).
4. Chen, Y. et al. Deciphering the molecular characteristics of human idiopathic nonobstructive azoospermia from the perspective of germ cells. *Adv. Sci.* **10**, e2206852 (2023).
5. Yuan, Y. et al. Generation of fertile offspring from Kit(w)/Kit(wv) mice through differentiation of gene corrected nuclear transfer embryonic stem cells. *Cell Res.* **25**, 851–863 (2015).
6. Hermo, L., Pelletier, R. M., Cyr, D. G. & Smith, C. E. Surfing the wave, cycle, life history, and genes/proteins expressed by testicular germ cells. Part 1: background to spermatogenesis, spermatogonia, and spermatocytes. *Microsc. Res. Tech.* **73**, 241–278 (2010).
7. Cavallini, G. Male idiopathic oligoasthenoteratozoospermia. *Asian J. Androl.* **8**, 143–157 (2006).
8. Yan, W. Male infertility caused by spermiogenic defects: lessons from gene knockouts. *Mol. Cell Endocrinol.* **306**, 24–32 (2009).
9. Kang, J. Y. et al. LLPS of FXR1 drives spermiogenesis by activating translation of stored mRNAs. *Science* **377**, eabj6647 (2022).
10. Sharma, A., Minhas, S., Dhillo, W. S. & Jayasena, C. N. Male infertility due to testicular disorders. *J. Clin. Endocrinol. Metab.* **106**, e442–e459 (2021).
11. Jan, S. Z. et al. Unraveling transcriptome dynamics in human spermatogenesis. *Development* **144**, 3659–3673 (2017).
12. Avidor-Reiss, T. & Fishman, E. L. It takes two (centrioles) to tango. *Reproduction* **157**, R33–r51 (2019).
13. Avasthi, P. et al. Germline deletion of Cetn1 causes infertility in male mice. *J. Cell Sci.* **126**, 3204–3213 (2013).
14. Cha, K. B. et al. Skeletal dysplasia and male infertility locus on mouse chromosome 9. *Genomics* **83**, 951–960 (2004).
15. Zhu, T. et al. Absence of CEP78 causes photoreceptor and sperm flagella impairments in mice and a human individual. *Elife* **12**, e76157 (2023).
16. Zhang, X. et al. Loss-of-function mutations in CEP78 cause male infertility in humans and mice. *Sci. Adv.* **8**, eabn0968 (2022).
17. Liu, Q. et al. Loss of CEP70 function affects acrosome biogenesis and flagella formation during spermiogenesis. *Cell Death Dis.* **12**, 478 (2021).
18. Sha, Y. W. et al. A homozygous CEP135 mutation is associated with multiple morphological abnormalities of the sperm flagella (MMAF). *Gene* **633**, 48–53 (2017).
19. Hall, E. A. et al. Acute versus chronic loss of mammalian Azi1/Cep131 results in distinct ciliary phenotypes. *PLoS Genet.* **9**, e1003928 (2013).
20. Kierszenbaum, A. L., Rivkin, E. & Tres, L. L. Cytoskeletal track selection during cargo transport in spermatids is relevant to male fertility. *Spermatogenesis* **1**, 221–230 (2011).
21. Khanal, S. et al. The evolution of centriole degradation in mouse sperm. *Nat. Commun.* **15**, 117 (2024).
22. Kodani, A. et al. Centriolar satellites assemble centrosomal microcephaly proteins to recruit CDK2 and promote centriole duplication. *Elife* **4**, e07519 (2015).
23. Bärenz, F., Mayilo, D. & Gruss, O. J. Centriolar satellites: busy orbits around the centrosome. *Eur. J. Cell Biol.* **90**, 983–989 (2011).
24. Moser, J. J., Fritzler, M. J., Ou, Y. & Rattner, J. B. The PCM-basal body/primary cilium coalition. *Semin. Cell Dev. Biol.* **21**, 148–155 (2010).
25. Gheiratmand, L. et al. Spatial and proteomic profiling reveals centrosome-independent features of centriolar satellites. *EMBO J.* **38**, e101109 (2019).

26. Fokin Artem, I., Zhapparova Olga, N., Burakov Anton, V. & Nadezhdina Elena, S. Centrosome-derived microtubule radial array, PCM-1 protein, and primary cilia formation. *Protoplasma* **256**, 1361–1373 (2019).

27. Wang, L., Lee, K., Malonis, R., Sanchez, I. & Dynlacht, B. D. Tethering of an E3 ligase by PCM1 regulates the abundance of centrosomal KIAA0586/Talpid3 and promotes ciliogenesis. *Elife* **5**, e12950 (2016).

28. Hall, E. A. et al. Centriolar satellites expedite mother centriole remodeling to promote ciliogenesis. *Elife* **12**, e79299 (2023).

29. Odabasi, E., Gul, S., Kavakli, I. H. & Firat-Karalar, E. N. Centriolar satellites are required for efficient ciliogenesis and ciliary content regulation. *EMBO Rep.* **20**, e47723 (2019).

30. Monroe, T. O. et al. PCM1 is necessary for focal ciliary integrity and is a candidate for severe schizophrenia. *Nat. Commun.* **11**, 5903 (2020).

31. Lehti, M. S. & Sironen, A. Formation and function of the manchette and flagellum during spermatogenesis. *Reproduction* **151**, R43–R54 (2016).

32. Stowe, T. R., Wilkinson, C. J., Iqbal, A. & Stearns, T. The centriolar satellite proteins Cep72 and Cep290 interact and are required for recruitment of BBS proteins to the cilium. *Mol. Biol. Cell* **23**, 3322–3335 (2012).

33. Staples, C. J. et al. The centriolar satellite protein Cep131 is important for genome stability. *J. Cell Sci.* **125**, 4770–4779 (2012).

34. Kierszenbaum, A. L., Gil, M., Rivkin, E. & Tres, L. L. Ran, a GTP-binding protein involved in nucleocytoplasmic transport and microtubule nucleation, relocates from the manchette to the centrosome region during rat spermiogenesis. *Mol. Reprod. Dev.* **63**, 131–140 (2002).

35. Li, L. & Ran, J. Regulation of ciliary homeostasis by intraflagellar transport-independent kinesins. *Cell Death Dis.* **15**, 47 (2024).

36. Lo, J. C. et al. RAB-like 2 has an essential role in male fertility, sperm intra-flagellar transport, and tail assembly. *PLoS Genet.* **8**, e1002969 (2012).

37. Baker, S. A., Freeman, K., Luby-Phelps, K., Pazour, G. J. & Besharse, J. C. IFT20 links kinesin II with a mammalian intraflagellar transport complex that is conserved in motile flagella and sensory cilia. *J. Biol. Chem.* **278**, 34211–34218 (2003).

38. San Agustin, J. T., Pazour, G. J. & Witman, G. B. Intraflagellar transport is essential for mammalian spermiogenesis but is absent in mature sperm. *Mol. Biol. Cell* **26**, 4358–4372 (2015).

39. Jreijiri, F. et al. CCDC65, encoding a component of the axonemal Nexin-Dynein regulatory complex, is required for sperm flagellum structure in humans. *Clin. Genet.* **105**, 317–322 (2024).

40. Aprea, I. et al. Pathogenic gene variants in CCDC39, CCDC40, RSPH1, RSPH9, HYDIN, and SPEF2 cause defects of sperm flagella composition and male infertility. *Front. Genet.* **14**, 1117821 (2023).

41. Shi, X. et al. Biallelic variants in CCDC39 gene lead to primary ciliary dyskinesia and kartagener syndrome. *Biomed. Res. Int.* **2022**, 7130555 (2022).

42. Cao, H. et al. Downregulation of KIF2C and TEKT2 is associated with male infertility and testicular carcinoma. *Aging* **13**, 22898–22911 (2021).

43. Reilly, M. L. & Benmerah, A. Ciliary kinesins beyond IFT: cilium length, disassembly, cargo transport and signalling. *Biol. Cell* **111**, 79–94 (2019).

44. Ruiz-Reig, N. et al. KIF2A deficiency causes early-onset neurodegeneration. *Proc. Natl Acad. Sci. USA* **119**, e2209714119 (2022).

45. Zhang, W. et al. Modeling microcephaly with cerebral organoids reveals a WDR62-CEP170-KIF2A pathway promoting cilium disassembly in neural progenitors. *Nat. Commun.* **10**, 2612 (2019).

46. Miyamoto, T. et al. The microtubule-depolymerizing activity of a mitotic kinesin protein KIF2A drives primary cilia disassembly coupled with cell proliferation. *Cell Rep.* **10**, 664–673 (2015).

47. Cogné, B. et al. Mutations in the kinesin-2 motor KIF3B cause an autosomal-dominant ciliopathy. *Am. J. Hum. Genet.* **106**, 893–904 (2020).

48. Holdgaard, S. G. et al. Selective autophagy maintains centrosome integrity and accurate mitosis by turnover of centriolar satellites. *Nat. Commun.* **10**, 4176 (2019).

49. Chen, Z. et al. Loss of Cep72 affects the morphology of spermatozoa in mice. *Front. Physiol.* **13**, 948965 (2022).

50. Zhang, J. et al. Loss of DRC1 function leads to multiple morphological abnormalities of the sperm flagella and male infertility in human and mouse. *Hum. Mol. Genet.* **30**, 1996–2011 (2021).

51. Wang, X. et al. Tssk4 is essential for maintaining the structural integrity of sperm flagellum. *Mol. Hum. Reprod.* **21**, 136–145 (2015).

52. Su, D. et al. Mutation screening and association study of the TSSK4 Gene in Chinese infertile men with impaired spermatogenesis. *J. Androl.* **29**, 374–378 (2008).

53. Schatten, H. & Sun, Q. Y. The functional significance of centrosomes in mammalian meiosis, fertilization, development, nuclear transfer, and stem cell differentiation. *Environ. Mol. Mutagen* **50**, 620–636 (2009).

54. O'Donnell, L. & O'Bryan, M. K. Microtubules and spermatogenesis. *Semin. Cell Dev. Biol.* **30**, 45–54 (2014).

55. Ji, S. et al. OBOX regulates mouse zygotic genome activation and early development. *Nature* **620**, 1047–1053 (2023).

56. Avidor-Reiss, T., Carr, A. & Fishman, E. L. The sperm centrioles. *Mol. Cell Endocrinol.* **518**, 110987 (2020).

57. Xie, M. et al. Adenylate kinase 1 deficiency disrupts mouse sperm motility under conditions of energy stress. *Biol. Reprod.* **103**, 1121–1131 (2020).

58. Wu, Y. et al. Alleviation of endoplasmic reticulum stress protects against cisplatin-induced ovarian damage. *Reprod. Biol. Endocrinol.* **16**, 85 (2018).

59. Zhang, Z. et al. Intraflagellar transport protein IFT20 is essential for male fertility and spermiogenesis in mice. *Mol. Biol. Cell* **27**, 3705–3716 (2016).

60. Song, K. et al. Targeting APLN/APJ restores blood-testis barrier and improves spermatogenesis in murine and human diabetic models. *Nat. Commun.* **13**, 7335 (2022).

61. Yuan, S. et al. Spata6 is required for normal assembly of the sperm connecting piece and tight head-tail conjunction. *Proc. Natl Acad. Sci. USA* **112**, E430–E439 (2015).

62. Xiong, W., Shen, C. & Wang, Z. The molecular mechanisms underlying acrosome biogenesis elucidated by gene-manipulated mice†. *Biol. Reprod.* **105**, 789–807 (2021).

Acknowledgements

Author contributions

Z.G.C. and Z.C.H. designed the experiments. Z.C.H., C.Y.H. and R.D.Y. conducted the experiments and analyses. R.D.Y., X.X.C. and H.B.Z. helped with technical support, data verification and processing, and statistical analyses. M.Y.X. and K.M. contributed to image manipulation. S.P.R. and Y.G.Z. collected the data. X.Y.Z., W.Y.L., H.R.F., D.Y.C. and M.M.M.A. collected human specimens. Z.C.H. and Z.G.C. wrote the manuscript. X.J.K., C.Y.H. and H.L. reviewed the manuscript. All of the authors read and approved the final manuscript.

Competing interests

The authors declare no competing interests.

Additional information

Supplementary information The online version contains supplementary material available at https://doi.org/10.1038/s42003-025-08319-x.

Correspondence and requests for materials should be addressed to Hong Liu, Chuyu Huang, Xiangjin Kang or Zhenguo Chen.

Peer review information *Communications Biology* thanks Emma Hall, Jana Muronova, and the other anonymous reviewers for their contribution to the peer review of this work. Primary Handling Editors: Rosie Bunton-Stasyshyn and Dario Ummarino. A peer review file is available.

Reprints and permissions information is available at http://www.nature.com/reprints

Publisher's note Springer Nature remains neutral with regard to jurisdictional claims in published maps and institutional affiliations.

[1]Guangdong Provincial Key Laboratory of Construction and Detection in Tissue Engineering, Department of Cell Biology, School of Basic Medical Sciences, Southern Medical University, Guangzhou, Guangdong, PR China. [2]Department of Obstetrics and Gynecology, Key Laboratory for Major Obstetric Diseases of Guangdong Province, Key Laboratory of Reproduction and Genetics of Guangdong Higher Education Institutes, The Third Affiliated Hospital of Guangzhou Medical University, Guangzhou, Guangdong, PR China. [3]Medical School, Fuyang Normal University, Fuyang, Anhui, China. [4]Department of Biological Sciences, Faculty of Science, King Abdulaziz University, Jeddah, Saudi Arabia. [5]Reproductive Center, Affiliated Shenzhen Maternity & Child Healthcare Hospital, Southern Medical University (Shenzhen Maternity & Child Healthcare Hospital), Shenzhen, Guangdong, PR China. [6]Center for Reproductive Medicine, Department of Obstetrics and Gynecology, Nanfang Hospital, Southern Medical University, Guangzhou, PR China. [7]Department of Anesthesiology, Guangdong Provincial People's Hospital (Guangdong Academy of Medical Sciences), Southern Medical University, Guangzhou, Guangdong, China. [8]These authors contributed equally: Zicong Huang, Runduan Yi, Xixian Cen. [9]These authors jointly supervised this work: Hong Liu, Chuyu Huang, Xiangjin Kang, Zhenguo Chen. ✉e-mail: zlhhong@126.com; 649876032@qq.com; xiangjinkang@gzhmu.edu.cn; czg1984@smu.edu.cn